Global ocean surface heat fluxes derived from the maximum entropy production framework accounting for ocean heat storage and Bowen ratio adjustments

Yong Yang[1], Huaiwei Sun[1,2,3,4*], Jingfeng Wang[5], Wenxin Zhang[6*], Gang Zhao[7], Weiguang Wang[8], Lei Cheng[9], Lu Chen[1], Hui Qin[1], Zhanzhang Cai[6]

[1]School of Civil and Hydraulic Engineering, Huazhong University of Science and Technology, Wuhan 430074, China

[2]Hubei Key Laboratory of Digital River Basin Science and Technology, Huazhong University of Science and Technology, Wuhan 430074, China

[3]Institute of Water Resources and Hydropower, Huazhong University of Science and Technology, Wuhan 430074, China

[4]College of Water Conservancy and Architectural Engineering, Shihezi University, Shihezi 832003, China

[5.]School of Civil and Environmental Engineering, Georgia Institute of Technology, Atlanta 30318, USA

[6.]Department of Physical Geography and Ecosystem Science, Lund University, Lund 22100, Sweden

[7.]Key Laboratory of Water Cycle and Related Land Surface Processes, Institute of Geographic Sciences and Natural Resources Research, Chinese Academy of Sciences, Beijing 100101, China

[8.]College of Hydrology and Water Resources, Hohai University, Nanjing 210098, China

[9.]State Key Laboratory of Water Resources and Hydropower Engineering Science, Wuhan University, Wuhan 430074, China

Correspondence to: Huaiwei Sun (hsun@hust.edu.cn) and Wenxin Zhang (wenxin.zhang@nateko.lu.se)

Abstract. Ocean evaporation, represented by latent heat flux (*LE*), plays a crucial role in global precipitation patterns, water cycle dynamics, and energy exchange processes. However, existing bulk methods for quantifying ocean evaporation are associated with considerable uncertainties. The Maximum Entropy Production (MEP) theory provides a novel framework for estimating surface heat fluxes, but its application over ocean surfaces remains largely unvalidated. Given the substantial heat storage capacity of the deep ocean, which can create temporal mismatches between variations in heat fluxes and radiation, it is crucial to account for heat storage when estimating heat fluxes. This study derived global ocean heat fluxes using the MEP theory, incorporating the effects of heat storage and adjustments to the Bowen ratio (the ratio of sensible heat to latent heat). We utilized multi-source data from seven auxiliary turbulent flux datasets and 129 globally distributed buoy stations to refine and validate the MEP model. The model was first evaluated using observed data from buoy stations, and the Bowen ratio formula that most effectively enhances the model performance was identified. By incorporating the heat storage effect and adjusting the Bowen ratio within the MEP model, the accuracy of the estimated heat fluxes was significantly improved, achieving an R^2 of 0.99 (regression

34 slope: 0.97) and a root mean squared error (RMSE) of 4.7 $W·m^{-2}$ compared to observations. The improved

35 MEP method successfully addressed the underestimation of *LE* and the overestimation of sensible heat by

36 the original model, providing new global estimates of *LE* at 93 $W·m^{-2}$ and sensible heat at 12 $W·m^{-2}$ for the

37 annual average from 1988 to 2017. Compared to the 129 buoy stations, the MEP-derived global *LE* dataset

38 achieved the highest accuracy, with a mean error (ME) of 1.3 $W·m^{-2}$, an RMSE of 15.9 $W·m^{-2}$, and a Kling-

39 Gupta Efficiency (KGE) of 0.89, outperforming four major long-term global heat flux datasets, including J-

40 OFURO3, ERA5, MERRA2, and OAFlux. Analysis of long-term trends revealed a significant increase in

41 global ocean evaporation from 1988 to 2010 at a rate of 3.58 $mm·yr^{-1}$, followed by a decline at -2.18 $mm·yr^{-1}$

42 ^{1} from 2010 to 2017. This dataset provides a new benchmark for the ocean surface energy budget and is

43 expected to be a valuable resource for studies on global ocean warming, sea surface-atmosphere energy

44 exchange, the water cycle, and climate change. The 0.25° monthly global ocean heat flux dataset based on

45 the Maximum Entropy Production method (GOHF-MEP) for 1988–2017, is publicly accessible at

46 https://doi.org/10.6084/m9.figshare.26861767.v2 (Yang et al., 2024; last accessed: 28 August 2024).

47 **1. Introduction**

48 The ocean system plays a pivotal role in regulating the global climate by receiving and redistributing heat

49 and freshwater, thereby influencing Earth's energy balance and the dynamics of the water cycle (Li et al.,

50 2023; Von Schuckmann et al., 2023; Marti et al., 2022; Johnson et al., 2020). A key component in this system

51 is ocean evaporation, which accounts for approximately 86% of atmospheric water vapor, being the primary

52 driver of the global hydrological cycle (Yu, 2011). As climate change warms the ocean, evaporation rates are

53 expected to rise, potentially intensifying the global hydrological cycle (Masson-Delmotte et al., 2021). This

54 intensification could alter precipitation patterns, affecting regional water availability and freshwater

55 ecosystems (Konapala et al., 2020; Roderick et al., 2014). Therefore, precise estimation of ocean evaporation

56 is critical to understand and quantify the global energy and water budget (Iwasaki et al., 2014).

57 Existing methods for calculating surface latent heat (*LE*) and sensible heat flux (*H*) rely on bulk transfer

58 formulations, which require extensive input variables and parameterizations, such as temperature gradients,

59 humidity gradients, wind speed, and transfer coefficients (Fairall et al., 1996; Andreas et al., 2008). Although

60 widely used, these bulk methods encounter significant limitations primarily due to challenges in accurately

61 parameterizing and empirically deriving transfer coefficients (Zeng et al., 1998; Robertson et al., 2020).

62 These methods heavily depend on assumptions regarding atmospheric stability and boundary layer dynamics,

63 which may not consistently apply across diverse and complex environmental conditions (Fairall et al., 2003;

64   Andreas et al., 2013). Furthermore, uncertainties in estimating turbulent transfer coefficients can lead to

65   substantial errors in the estimation of latent heat flux. The high demands for parameterization and challenges

66   in data acquisition contribute to considerable uncertainties when implementing bulk methods for calculations.

67   While numerous energy balance-based algorithms have been developed to estimate global terrestrial

68   evapotranspiration (Wang et al., 2012; Yang et al., 2023), their application to ocean surface heat flux

69   estimation remains limited. Therefore, proposing an innovative method for estimating ocean surface heat flux

70   based on surface energy balance could yield significant theoretical and practical implications. Such an

71   approach could serve as a valuable complement to existing bulk methods and their associated datasets,

72   providing a fresh methodological perspective for quantifying ocean heat flux. This advancement would not

73   only enhance our ability to estimate ocean energy fluxes with greater accuracy but also deepen our

74   understanding of their role in the global energy and water cycles.

75   The Maximum Entropy Production (MEP) model, an energy-balance-based approach, has recently

76   emerged as a novel method for simulating surface heat fluxes. Developed from Bayesian probability theory

77   and information theory, the MEP prioritizes the most probable partitioning of radiation fluxes (Wang & Bras,

78   2011). The MEP model has been rigorously validated across diverse surface types and varying degrees of

79   surface wetness (Wang et al., 2014; Huang et al., 2017; Yang et al., 2022; Sun et al., 2022; Sun et al., 2023).

80   Notably, the MEP model requires fewer input variables—net radiation, surface temperature, and specific

81   humidity—yet provides accurate estimates of LE, H, and ground heat fluxes simultaneously. Unlike bulk

82   methods (Fairall et al., 2003), which rely on wind speed, temperature gradient, and humidity gradient, the

83   MEP model satisfies the energy balance constraint without these dependencies. This characteristic enhances

84   its applicability and robustness across diverse environmental conditions. However, the previous application

85   of the MEP model over ocean surfaces has revealed significant limitations, including notable

86   underestimations of latent heat and overestimations of H (Huang et al., 2017). The global multi-year averaged

87   LE estimated by the MEP model indicated a value around 58 $W \cdot m^{-2}$, much lower than the range of 92~109

88   $W \cdot m^{-2}$ reported by remote sensing or reanalysis-based products. Conversely, MEP estimated an averaged H

89   of approximately 28 $W \cdot m^{-2}$, substantially higher the 6-18 $W \cdot m^{-2}$ range reported in other studies. These

90   discrepancies highlight substantial uncertainties in applying the MEP model to oceanic energy partitioning,

91   highlighting the urgent need for further refinement and rigorous validation. These substantial errors in MEP-

estimated oceanic fluxes may be attributed to the lack of consideration of heat storage effects. The significant impact of heat storage in deep ocean water can introduce substantial bias in estimating seasonal evaporation rates when using the Penman combination-based method (McMahon et al., 2013; Bai & Wang et al., 2023). For instance, deep-water bodies typically store heat during the spring and release it in the fall, which can lead to overestimation of evaporation in the summer and underestimation in the fall if changes in heat storage are not accounted for (Zhao & Gao, 2019; Morton, 1994). Therefore, when estimating heat fluxes using the Bowen ratio (B_o, defined as the ratio of H to LE) energy budget-based method (including the MEP method), it is essential to incorporate heat storage effects to ensure accurate partitioning of available energy.

B_o is crucial for understanding the global ocean energy partitioning process (Hicks & Hess, 1977). In the context of the energy balance-based MEP model, the significant overestimation of B_o suggests that focusing on this ratio can enhance our understanding of energy partitioning dynamics (Andreas et al., 1996). Studies have highlighted that the actual Bowen ratio over ocean surfaces (B_{oa}) often diverges from the equilibrium Bowen ratio (B_o^*) observed under ideal conditions where the air is saturated with water vapor. The B_{oa} may deviate significantly from B_o^* under non-equilibrium conditions, which are typical in most environments (Jo et al., 2002; Andreas et al., 2013), posing challenges in establishing a robust relationship between B_{oa} and B_o^* (Liu & Yang, 2021). Therefore, developing an accurate $B_o^* \sim B_{oa}$ relationship is crucial for refining the energy partitioning process in the MEP model. The advancement of buoy observation networks has provided compelling evidence for validating ocean heat fluxes and become crucial in assessing their associated uncertainties (Bourras, 2006; Smith et al., 2011; Bentamy et al., 2017; Liang et al., 2022). This study utilizes the energy balance-based MEP method to estimate ocean evaporation, introducing a novel approach to redistributing surface energy budgets and offering a streamlined parameterization scheme distinct from conventional bulk methods used for estimating ocean heat fluxes. In contrast to existing approaches that using reanalysis-based schemes (e.g., NCEP, ECMWF, and GEOS) and their associated parameterizations to estimate LE, this study employs satellite observations to directly estimate ocean heat fluxes, thereby minimizing error propagation associated with the model structures and assimilation schemes.

Current global ocean surface heat flux datasets can be classified into five categories based on their deriving approaches (Tang et al., 2023): remote sensing-based (e.g., J-OFURO3), atmospheric reanalysis-based (e.g., ERA5), machine learning-based (e.g., OHFv2), in-situ based (e.g., NOC), and hybrid-based (e.g.,

120   OAFlux) approaches. Compared to terrestrial flux products, these ocean flux products generally have a

121   coarser spatial resolution ranging from 0.25° to 1.875°. Recent studies have conducted comprehensive

122   assessments of global ocean heat flux datasets regarding their accuracy and error characteristics across spatial

123   and temporal scales (Bentamy et al., 2017; Tang et al., 2023). However, substantial discrepancies remain

124   among these datasets, particularly in terms of spatial patterns, annual means, and interannual variabilities.

125   Therefore, developing a new global dataset using the innovative method could advance our understanding of

126   deriving algorithms, improve temporal and spatial coverage of flux variables with a higher accuracy, and

127   provide alternative reference to assess ocean surface heat fluxes in various applications. The primary

128   objectives of this study are as follows: (1) to develop and validate the MEP approach for estimating ocean

129   heat fluxes using observations from 129 stations; (2) to investigate the impact of heat storage on ocean energy

130   allocation and the influence of the Bowen ratio on energy partitioning for heat flux estimations; (3) to produce

131   a MEP-derived ocean heat fluxes product (spatial resolution: 0.25°; temporal coverage: 1988-2017) and

132   present its spatiotemporal patterns.

133   **2. Methods**

134   **2.1 Components of ocean surface energy balance**

135   The global ocean energy balance equation is as follows (Meehl, 1984; Wang et al., 2021):

136
$$R_n = LE + H + G \tag{1}$$

137
$$R_n = R_{ns} + R_{nl} = R_s^{\downarrow} - R_s^{\uparrow} + R_l^{\downarrow} - R_l^{\uparrow} \tag{2}$$

138   where R_n, R_{ns}, and R_{nl} are net radiation, net shortwave radiation (the difference of incoming radiation

139    $R_s^{\downarrow}$ and reflected solar radiation $R_s^{\uparrow}$), and net longwave radiation (the difference of incoming longwave

140   radiation $R_l^{\downarrow}$ and outgoing longwave radiation $R_l^{\uparrow}$), respectively; H is sensible heat, LE is latent heat, and

141   G is the heat flow through the surface. Unlike terrestrial surfaces, the energy balance equation for the ocean

142   surface accounts for distinct energy exchange processes, including the impact of seawater mixing and

143   dynamics on energy transfer. For the ocean surface, the flux term G has two components,

144
$$G = G_t + G_v \tag{3}$$

145 where G_t is the change in the ocean heat content (ΔOHC, or heat storage), and G_v is the lateral heat

146 transported by ocean currents and other processes. The G_t can be quantified as the vertical integration of

147 temperature profile in a column of depth (Meehl, 1984, Li et al., 2023). Both the heat storage and the ocean

148 heat transport G_v are difficult to quantify, which requires large masses of hydrographic variables and

149 performing integrations at different depths. Since the lateral heat transport by ocean currents is zero at the

150 global scale (Wang et al., 2021), G can be regarded as equivalent to the change in ocean heat content or heat

151 storage at the global level. For the consistency throughout the paper, this study will consider the concept of

152 G flux as equivalent to the changes in the heat storage.

153 **2.2 The Maximum Entropy Production theory**

154 2.2.1 The original MEP model

155 The MEP model simulates ocean surface heat fluxes using inputs variables of net radiation (R_n), surface skin

156 temperature (T_s), and surface specific humidity (q_s) under the constraint of the surface energy balance. The

157 latent heat, sensible heat, and surface thermal energy flux (Q) are calculated as,

$$[1+B(\sigma)+\frac{B(\sigma)}{\sigma}\frac{I_s}{I_0}|H|^{-\frac{1}{6}}]H = R_n \tag{4}$$

$$E = B(\sigma)H \tag{5}$$

$$Q = R_{nl} - E - H \tag{6}$$

$$B(\sigma) = 6(\sqrt{1+\frac{11}{36}\sigma}-1), \quad \sigma = \frac{\lambda^2}{c_p R_v}\frac{q_s}{T_s^2} \tag{7}$$

$$I_0 = \rho_a c_p \sqrt{C_1 kz}(C_2 \frac{kzg}{\rho_a c_p T_r})^{\frac{1}{6}} \tag{8}$$

163 where $B(\sigma)$ is the reciprocal Bowen ratio, σ is a dimensionless parameter that characterizes the phase

164 change at the ocean surface, λ (J·kg⁻¹) is the latent heat of vaporization of liquid surface, c_p (10³ J·kg⁻¹·K⁻¹)

165 is the specific heat of air under constant pressure, and R_v (461 J·kg⁻¹·K⁻¹) is the gas constant of water vapor.

166 I_0 is the "apparent thermal inertia" of air and describes the turbulent transport process of the boundary layer

167   based on the Monin-Obukhov similarity theory (MOST) (Wang and Bras, 2010). I_s is the thermal inertia of

168   the ocean surface (J·m^{-2}·K^{-1}·s$^{-1/2}$), and can be parametrized as $I_s = \sqrt{\rho c \lambda}$ (with density ρ, the specific

169   heat c) represents the physical property of surface ($I_s = 1.56 \times 10^3$ J·m^{-2}·K^{-1}·s$^{-1/2}$ for water surface and

170   1.92×10^3 J·m^{-2}·K^{-1}·s$^{-1/2}$ for ice surface).

171   Over the sea ice surface, assumed to be saturated, the specific humidity q_s can be derived as a function

172   of surface temperature T_s using the Clausius-Clapeyron equation. (El Sharif et al., 2019; Shaman & Kohn,

173   2009).

$$q_s = \varepsilon \frac{e_s(T_s)}{P} = \varepsilon \frac{e_0}{P} \exp[\frac{\lambda_s}{R_v}(\frac{1}{T_0} - \frac{1}{T_s})] \tag{9}$$

175   where ε (= 0.622) represents the ratio of the molecular weight of water vapor to that of dry air, $e_s(T_s)$

176   denotes the saturation vapor pressure at temperature Ts, e_0 is the saturation vapor pressure at the reference

177   temperature T_0 (273.15 K), and P is the atmospheric pressure (mb).

178   2.2.2 Specific improvements on the MEP model

179   According to the MEP theory, the net solar radiation (R_{ns}) entering the water surface medium is absorbed by

180   the water body, with the allocable radiation flux denoted as $R_{nl} = E + H + Q$ (Eq.6). Consequently, the

181   expression for ocean heat uptake (heat storage) is derived as $G = R_n - E - H = R_{ns} + Q$. While this theory

182   has received preliminary validation in shallower water bodies, such as lake surfaces (Wang et al., 2014), its

183   applicability on deeper water bodies with larger heat storage capacities in ocean surfaces requires further

184   evaluation. This study introduced two key hypotheses: (1) The substantial heat storage capacity of the ocean

185   could exert a significant influence on seasonal latent and sensible fluxes, potentially introducing bias to the

186   MEP equations, (2) The notable underestimation of latent heat flux and overestimation of sensible heat flux

187   by the MEP model point to a significant deviation from the Bowen's ratio formula, necessitating a reasonable

188   correction. To address this, the study proposed two approaches for enhancing the MEP formulas: (1)

189   Considering the impact of heat storage in the MEP's energy balance equation, and (2) Adjusting the

190   theoretical equilibrium Bowen ratio within the MEP model. This can be specifically represented as follows:

191
$$[1+\frac{1}{B_o^*}]H = R_n - G \tag{10}$$

192
$$B_o^* = \frac{1}{B(\sigma)} \tag{11}$$

193
$$B_{oa} = a \times B_o^* + b \tag{12}$$

194 where B_o^* is the equilibrium Bowen ratio, which denotes the theoretical ratio of sensible heat flux to latent

195 heat flux when the surface and the atmosphere are in equilibrium regarding water vapor. Correspondingly,

196 the corresponding evaporation at this condition is known as equilibrium evaporation (defined as the water

197 vapor evaporating from a saturated surface into a saturated atmosphere). To accurately predict actual

198 evaporation, a reliable functional relationship needs to be established to predict B_{oa} from B_o^*. Empirical

199 studies have introduced coefficients to correlate B_o^* to B_{oa} under diverse environmental circumstances; for

200 instance, the Priestley–Taylor coefficient was expressed as (Priestley & Taylor, 1972).

201
$$B_{oa} = 0.79 \times B_o^* - 0.21 = \frac{0.79 - 0.21 \times B(\sigma)}{B(\sigma)} \tag{13}$$

202 Further studies have led to the emergence of more updated empirical coefficients. Hicks and Hess (1977)

203 estimated the actual Bowen ratio as $B_{oa} = 0.63 \times B_o^* - 0.15$ by aligning it with direct observations of the

204 fluxes. Yang & Roderick (2019) deduced an empirical coefficient of 0.24 and formulated it as

205 $B_{oa} = 0.24 \times B_o^*$ through fitting Bowen ratio and surface temperature data across the global ocean surface.

206 Furthermore, Liu & Yang (2021) derived a new equation as $B_{oa} = 0.37 \times B_o^* - 0.05$ based on the

207 atmospheric boundary layer model. Given their favorable spatial applicability and representativeness, this

208 study opted to utilize these four $B_{oa} \sim B_o^*$ formulas to refine the MEP model and assess their suitability. The

209 revised reciprocal actual Bowen ratio was represented as,

210
$$\left.\begin{cases} B(\sigma)_{a1} = \dfrac{1}{B_{oa}} = \dfrac{B(\sigma)}{0.79 - 0.21 \times B(\sigma)} \\[2ex] B(\sigma)_{a2} = \dfrac{1}{B_{oa}} = \dfrac{B(\sigma)}{0.63 - 0.15 \times B(\sigma)} \\[2ex] B(\sigma)_{a3} = \dfrac{1}{B_{oa}} = \dfrac{B(\sigma)}{0.24} \\[2ex] B(\sigma)_{a4} = \dfrac{1}{B_{oa}} = \dfrac{B(\sigma)}{0.37 - 0.05 \times B(\sigma)} \end{cases}\right\}$$
(14)

211 where $B(\sigma)_{a1} \sim B(\sigma)_{a4}$ represent the four empirical Bowen ratio formulas for comparisons in this study.

212 Thus, the workflow of the improved MEP model was conducted as: replacing the original $B(\sigma)$ with

213 the corrected $B(\sigma)_a$, then combining Eq. (5), (7)-(9), and (14) into the MEP energy balance equation

214 considering heat storage (Eq. (10)), ultimately leading to the determination of latent and sensible heat flux.

215 **2.3 Sensitivity analysis**

216 To quantify the influence of input variables in the MEP model on evaporation estimate at the ocean surface,

217 the sensitivity coefficient (S) was computed as (Beven, 1979; Isabelle et al., 2021),

218
$$S_i = \frac{\partial LE}{\partial x_i} \frac{x_i}{LE}$$
(15)

219 where S_i represents the sensitivity coefficient of LE to each variable x_i. The magnitude of S_i reflects the degree

220 of impact of the variable's changes on LE; a larger absolute value indicates a greater influence of the variable

221 on LE. A positive value signifies a positive correlation between evaporation and the variable's changes, while

222 a negative value indicates a negative correlation. For example, a sensitivity coefficient of 0.5 represents that

223 a 10% increase in the variable would result in a 5% increase in LE. The sensitivity levels can be categorized

224 based on the absolute value |Si| (Lenhart et al., 2002; Yin et al., 2010): |Si| > 1 indicates very high sensitivity,

225 1 > |Si| > 0.2 denotes high sensitivity, 0.2 > |Si| > 0.05 reflects moderate sensitivity, and |Si| < 0.05 suggests

226 negligible sensitivity.

227 **2.4 Data fusion methods**

228 To drive the improved MEP model with high-quality input data, this study aims to obtain a heat storage

229 dataset with optimal accuracy. The accuracy of the heat storage dataset was assessed using three approaches:

230 (1) individual dataset, (2) a fused dataset generated using the Bayesian Three-Cornered Hat (BTCH) method

231 (He et al., 2020), and (3) an ensemble means obtained through the arithmetic average (AA) method. Previous

232 studies have demonstrated that the BTCH method effectively quantifies uncertainties across diverse datasets

233 and improves accuracy by integrating multiple datasets without requiring prior knowledge (Long et al., 2017;

234 Liu et al., 2021; Duan et al., 2024). A recent study further evaluated various data fusion methods, including

235 BTCH and the AA method, for addressing uncertainties in global evapotranspiration estimates derived from

236 different datasets. The findings revealed that while both BTCH and AA are effective in identifying lower-

237 quality ET datasets, their ability to consistently produce higher-accuracy datasets remains uncertain and, in

238 some cases, may even degrade the overall accuracy (Shao et al., 2022). The performance of these fusion

239 methods is highly sensitive to the selection of input datasets. For instance, the AA method is particularly

240 susceptible to the influence of lower-quality datasets, especially when the sample size is small. Similarly, the

241 performance of BTCH diminishes as the error covariance among the included datasets increases.

242 Consequently, following a comparative analysis of the accuracy of individual, BTCH, and AA fusion datasets,

243 this study selected the optimal heat storage dataset to drive the MEP model. Since BTCH is not the primary

244 focus of this study, detailed method descriptions are referred to He et al. (2020).

245 **3. Data materials**

246 **3.1 Input data for MEP model**

247 The performance of both the original and improved Maximum Entropy Production (MEP) models was

248 evaluated using observed data from in-situ buoy stations, as described in Section 3.2. The optimal empirical

249 Bowen ratio formula for the MEP model was then determined through multi-site assessments. Subsequently,

250 the improved MEP model was applied to estimate global heat fluxes using long-term remote sensing data, as

251 detailed in Sections 3.3 and 3.4. Specifically, the input variables of net radiation, heat storage, and sea surface

252 temperature driving the improved MEP model were derived from the J-OFURO3 dataset, spanning 1988 to

253 2017 with a spatial resolution of 0.25°, as outlined in Section 4.3.

254 **3.2 In situ buoy observations**

255 A total of 129 in situ buoy sites were employed for ocean heat fluxes calculation and validation with MEP

256 model and its modified version, as listed in Table 1. About 96% of selected sites (124 of 129 all sites) were

collected from the Global Tropical Moored Buoy Array (available at https://www.pmel.noaa.gov/), which consists of the TAO/TRION Pacific Ocean (69 buoys), PIRATA Atlantic Ocean (23 buoys), and RAMA Indian ocean (32 buoys), and the remaining sites including Upper Ocean Processes Group (3 buoys) consists of Project WHOTS - WHOI Hawaii Ocean Time-series Station (available at https://uop.whoi.edu/ReferenceDataSets/whotsreference.html), Project NTAS - Northwest Tropical Atlantic Station and Project STRATUS (https://uop.whoi.edu/ReferenceDataSets/ntasreference.html), and the Pacific ocean climate stations (2 buoys) consists of KEO and PAPA moorings (https://www.pmel.noaa.gov/ocs/data/fluxdisdel/). The availability of all buoy stations refers to the "Data availability" section. The observational sites covered the spatial range of 25°S~ 50.1°N latitude, temporal range span from 1989/12 to 2023/12. Observational meteorological variables and heat fluxes included the net longwave radiation, net shortwave radiation, sea surface skin temperature, specific humidity at 2m height (if available, or computed as the function of SST according to the Clausius‑Clapeyron equation), latent heat flux and sensible heat flux. Limited by the availability of longwave radiation observations, the net radiation had a relatively shorter time series length compared to latent and sensible heat fluxes. The surface air-sea fluxes of buoy observations were computed using the COARE 3.0b algorithm, which have been widely applied for fluxes estimations and validations (Tang et al., 2023; Bentamy et al., 2017; Fairall et al., 2003). All the selected original buoy observation (except for KEO and Papa sites) records were in monthly temporal resolution, and the original daily observations of KEO and Papa had been aggregated to monthly by simple average method. The spatially distributed map of all selected sites was illustrated in Fig.S1.

Table 1. Information about observational ocean surface heat fluxes of 129 buoy sites

Buoy array	Buoy amount	Spatial coverage	Temporal coverage	Number of LE (H) records	Number of R_n records
TAO/TRION pacific	69	165°E-95°W 10°S-10°N	1989/12/16-2023/12/16	12377	522
PIRATA Atlantic	23	40°W-10°E, 20°S-20°N	1997/9/16-2023/12/16	2644	631
RAMA Indian	32	55°E-100°E, 25°S-15°N	2001/11/16-2023/12/16	1862	286
WHOTS	1	158°W, 22.7°N	2004/08/15-2021/08/15	205	205

NTAS	1	51°W, 15°N	2001-04/15-2020/03/15	219	219
STRATUS	1	85.4°W, 19.6°S	2000/10/15-2021/01/15	235	235
KEO	1	144.6°E, 32.3°N	2004/06/17-2023/08/12	177	177
PAPA	1	144.9°W, 50.1°N	2007/06/08-2023/11/14	181	181

Note: The number of records represents the effective count (excluding NA values) of latent and sensible heat flux observations.

3.3 Global turbulent heat flux datasets for evaluations

This study evaluated and compared 7 global turbulent heat flux products with observations, categorizing them into three types: Remote sensing-based, atmosphere reanalysis-based, and hybrid-based (Table 2). These seven products encompassed monthly data spanning from 1988 to 2017, with spatial resolutions ranging from 0.25° to 1°. The criterion for dataset filtering prioritized products with relatively long time series, typically exceeding 15 years.

The Clouds and Earth's Radiant Energy Systems Synoptic Edition 4A (CERES SYN1deg_Ed4A, hereafter referred to as CERES4, available at https://ceres.larc.nasa.gov/data/) offers net radiation data, derived from clear-sky upward shortwave, downward shortwave flux, upward longwave, and downward longwave flux measurements (Wielicki et al., 1996; Rutan et al., 2015). Another remote sensing-based radiation product, the Global Energy and Water Cycle Experiment - Surface Radiation Budget (GEWEX-SRB, available at https://asdc.larc.nasa.gov/project/SRB) (Pinker et al., 1992), in conjunction with CERES4, demonstrated good accuracy in retrieving R_n, as validated by six global observing networks (Liang et al., 2022).

The J-OFURO3 is the third-generation dataset developed by the Japanese Ocean Flux Data Sets with use of the Remote-Sensing Observations (J-OFURO) research project (available at https://j-ofuro.isee.nagoya-u.ac.jp/en/) (Tomita et al., 2019). It calculated turbulent heat flux with the latest version of COARE3.0 algorithm, and provided datasets for R_n, LE, H and SST in this study. Validation with in situ observations showed that J-OFURO3 offered a superior performance of latent heat compared to other 5 satellite products from 2002-2013 (Tomita et al., 2019).

300   Two Atmosphere reanalysis products including the fifth generation European Centre for Medium-Range

301   Weather Forecasts (ECMWF) atmospheric Re-Analysis52 (ERA5, available at

302   https://cds.climate.copernicus.eu/cdsapp#!/dataset/reanalysis-era5-single-levels-monthly-

303   means?tab=overview) (Hersbach et al., 2020), and the Modern-Era Retrospective analysis for Research and

304   Applications Version2 (MERRA2, available at

305   https://disc.gsfc.nasa.gov/datasets/M2TMNXOCN_5.12.4/summary) (Gelaro et al., 2017). Both ERA5 and

306   MERRA2 products employed the bulk formula based on the MOST to calculate heat fluxes. Validation

307   results from previous studies have demonstrated good consistency with buoy estimates regarding heat fluxes

308   (Pokhrel et al., 2020; Chen et al., 2020).

309   The OAFlux (available at https://oaflux.whoi.edu/), a hybrid-based product developed under the

310   Objectively Analyzed Air-Sea Fluxes (OAFlux) project at the Woods Hole Oceanographic Institution (WHOI)

311   (Yu et al., 2008), was utilized for comparisons with ocean heat fluxes derived from distinct methods. This

312   product calculates fluxes based on the COARE3.0 bulk algorithm and employs a variational objective

313   analysis to determine the optimal fitting of independent variables. Detailed descriptions on all utilized global

314   turbulent heat fluxes products, and their validation performances against buoy observations with reported

315   studies were available in Tang et al (2023).

316

317   **Table 2.** The information of the 7 used global radiation and heat fluxes products

Product	Variables	Spatial resolution	Time span	Type	Reference
CERES4	R_n	1°	2000-2017	Remote sensing	Rutan et al. (2015)
GEWEX-SRB	R_n	1°	1988-2017	Remote sensing	Pinker et al. (1992)
J-OFURO3	R_n, SST, LE, H	0.25°	1988-2017	Remote sensing	Tomita et al. (2019)
ERA5	R_n, LE, H, P	0.25°	1988-2017	Atmosphere reanalysis	Hersbach. et al. (2020)
MERRA2	R_n, LE, H	$1/2° \times 2/3°$	1988-2017	Atmosphere reanalysis	Gelaro et al. (2017)
OAFlux	LE, H	1°	1988-2017	Hybrid-based	Yu et al. (2008)
IAPv4-OHC	OHC	1°	1988-2017	Hybrid-based	Cheng et al. (2017)

318 **3.4 Ocean heat content data**

319 Remote sensing data for heat storage (G) was primarily derived from two categories: the first category

320 included data obtained from the residual of the energy balance equation (R_n-LE-H), including J-OFURO3,

321 ERA5, and MERRA2; the second category was calculated from changes in Ocean Heat Content (OHC). The

322 ocean heat content data was obtained from IAP OHC gridded analysis (IAPv4, available at

323 http://www.ocean.iap.ac.cn/) dataset, covering ocean depth of 0-6000m (Cheng et al., 2017), and has been

324 extensively utilized in global ocean heat analysis, ocean warming, and climate change studies (Li et al., 2023;

325 Cheng et al., 2022; Cheng et al., 2024). The delta OHC was calculated using the numerical differentiation

326 method (Xu et al., 2019) as $\Delta\text{OHC}(i) = \dfrac{OHC(i+1) - OHC(i-1)}{2\Delta i}$, i denotes the OHC of i-th month.

327 At the WHOTS site, this study compared the OHC changes at different depths with the observed G, derived

328 as Rn-LE-H (Table S1). Since the OHC variation from 0~100m depth exhibited the smallest error with the

329 observations, the data from 0~100m depth range were chosen as the heat storage. This study assessed the

330 suitability of G flux and ΔOHC for global evaporation estimations, with the aim of minimizing the errors

331 introduced by input variable data in the MEP model.

332 This study evaluated the accuracy of all the variables R_n, T_s, and G using the aforementioned datasets

333 on a global scale by comparing them against buoy observations (in Section 4.3), to optimize input accuracy

334 for driving the MEP model. To maintain consistency in the analysis, this study resampled all products to 1°

335 spatial resolution when comparing the Bowen ratio across multiple products. Nevertheless, when conducting

336 site validations with buoy observations, the original resolution of the data was preserved to minimize

337 uncertainty attributable to scale effects.

338 **4. Results**

339 **4.1 The new MEP model with heat storage and the revised Bowen ratio formulas**

340 To demonstrate how the MEP model has been developed and improved, we showed the comparisons of

341 different MEP models in simulating heat fluxes across 129 global buoy stations (Fig.1). Limited by the

342 availability of R_{nL} data, we used $LE + H$ instead of the available energy ($R_n - G$), enabling the utilization of

343 more observational records to verify the MEP model. The original MEP model (without considering heat

344   storage) showed a significant negative correlation between LE and H (with R^2 exceeding 0.65 as in Fig.1a &

345   Fig.1c), with considerable errors, where the RMSE of LE was 134.6 $W \cdot m^{-2}$ and that of H was 37 $W \cdot m^{-2}$.

346   After incorporating the influence of heat storage effects (represented as MEP_M, as depicted in Fig.1b and

347   Fig.1h), the MEP-simulated LE showed a good consistency with buoy observations, with an R^2 value of 0.97

348   and a reduced RMSE of 27 $W \cdot m^{-2}$. However, the MEP_M method revealed a significant bias in the

349   partitioning of LE and H from the available energy. Specifically, LE was underestimated by 25% (regression

350   slope = 0.75), while H was overestimated by 46% compared to observations. This finding agreed with

351   previous research findings that equilibrium evaporation tended to underestimate actual evaporation from

352   saturated surfaces by 20%~30% (Yang & Roderick, 2019; Philip, 1987). The significant difference between

353   B_{oa} and B_{o*} could exist as the equilibrium evaporation is considered as the lower limit of actual evaporation

354   from saturated surfaces (Priestley and Taylor, 1972). To address the deviation between B_{oa} and B_o^*, it is

355   necessary to convert the equilibrium Bowen ratio into the actual Bowen ratio, allowing for a more reasonable

356   and accurate allocation of surface energy budget.

357   After incorporating the effects of heat storage, four variants of the MEP model were developed by

358   replacing B_{o*} with B_{oa} derived from four different empirical formulas. These variants were defined as follows:

359    $M\_0.24$ (where $B_{oa}=0.24 B_o^*$), $M\_0.79$ (where $B_{oa}=0.79 B_o^*-0.21$), $M\_0.63$ (where $B_{oa}=0.63B_o^*-0.15$), and

360    $M\_0.37$ (where $B_{oa}=0.37B_o^*-0.05$). Adjusting the Bowen ratio significantly improved the accuracy of the

361   energy flux estimates. The simulated LE exhibited strong agreement with observations, with all R^2 exceeding

362   0.97 and RMSE ranging from 4.7 $W \cdot m^{-2}$ (for $M\_0.24$) to 7.1 $W \cdot m^{-2}$ (for $M\_0.79$), which was lower than that

363   derived from B_o^* (RMSE = 27 $W \cdot m^{-2}$). Both $M\_0.79$ and $M\_0.63$ tended to underestimate LE, especially

364   when LE exceeded 200 $W \cdot m^{-2}$ (Fig. 1d and Fig.1e). For the simulated H, the $M\_0.24$ outperformed the other

365   three, showing the smallest errors and highest R^2.

366

367
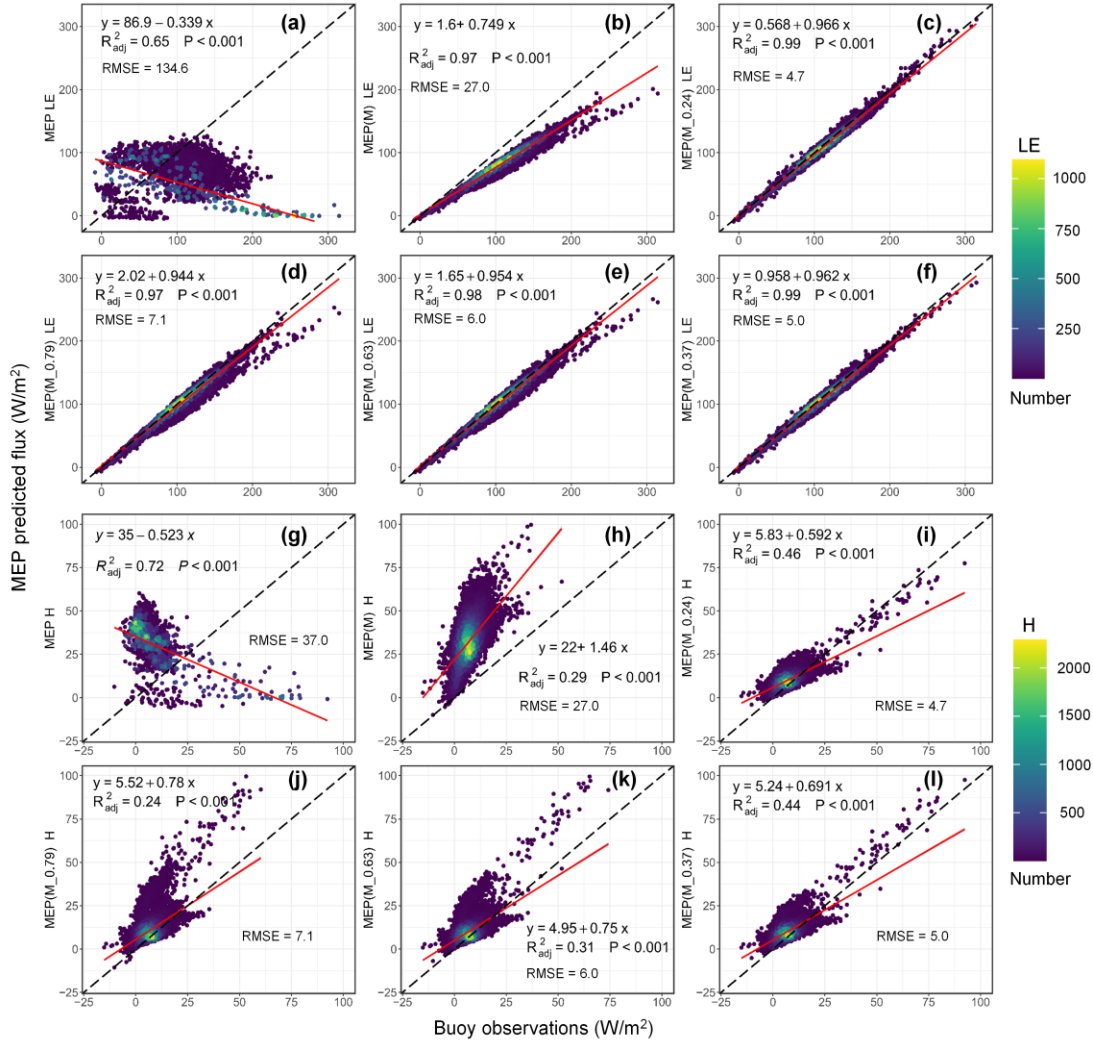
Figure 1. Scatter density plots of monthly latent heat flux (a~f) and sensible heat flux (g~l) derived by the original and modified MEP methods versus observations from 129 buoy stations (as in Table 1). (a) The original MEP method, (b) The modified MEP method considering the heat storage effect, (c) The modified MEP method considering both the heat storage and empirical Bowen ratio formula $B_{oa}=0.24B_o^*$, (d)~(f) for the modified MEP method considering both the heat storage and empirical Bowen ratio formulas $B_{oa}=0.79B_o^*-0.21$, $B_{oa}=0.63B_o^*-0.15$, and $B_{oa}=0.37B_o^*-0.05$. (g)~(l) are the same with (a)~(f) but for sensible heat flux.

Specifically, the spatial patterns of simulated errors for the four variants of the MEP model were obtained (Fig. 2), along with the errors across different observational buoy arrays (Fig. 3). Overall, the four variants of the improved MEP models demonstrated relatively lower bias at low latitudes (10°S to 10°N) but exhibit larger bias in higher latitude regions (above 15°N), particularly at the KEO, WHOTS, and STRATUS buoy sites. Comparing the four formulas across varying latitudes, the *M_0.24* formula exhibited the smallest RMSE (ranging from 3.6 to 12 W·m⁻²) (Fig. 3c), while the *M_0.79* formula showed the largest errors (RMSE

382   ranging from 3.9 to 26.6 W·m^{-2}). This consistency was also evident in the Kling-Gupta Efficiency (KGE)

383   coefficient, with *M_0.24* demonstrating superior performance in terms of accuracy, robustness, and

384   adaptability. In term of *M_0.24* formula, the prediction errors across observational arrays ranked as follows:

385   RAMA < PIRATA < TAO/TRION < PaPa < KEO < STRATUS < WHOTS < NTAS. The arrays with

386   relatively larger RMSE (NTAS in the Atlantic Ocean, WHOTS, and STRATUS in the Pacific Ocean) may

387   originate from the larger observed values of LE (Fig. S2).

388

389
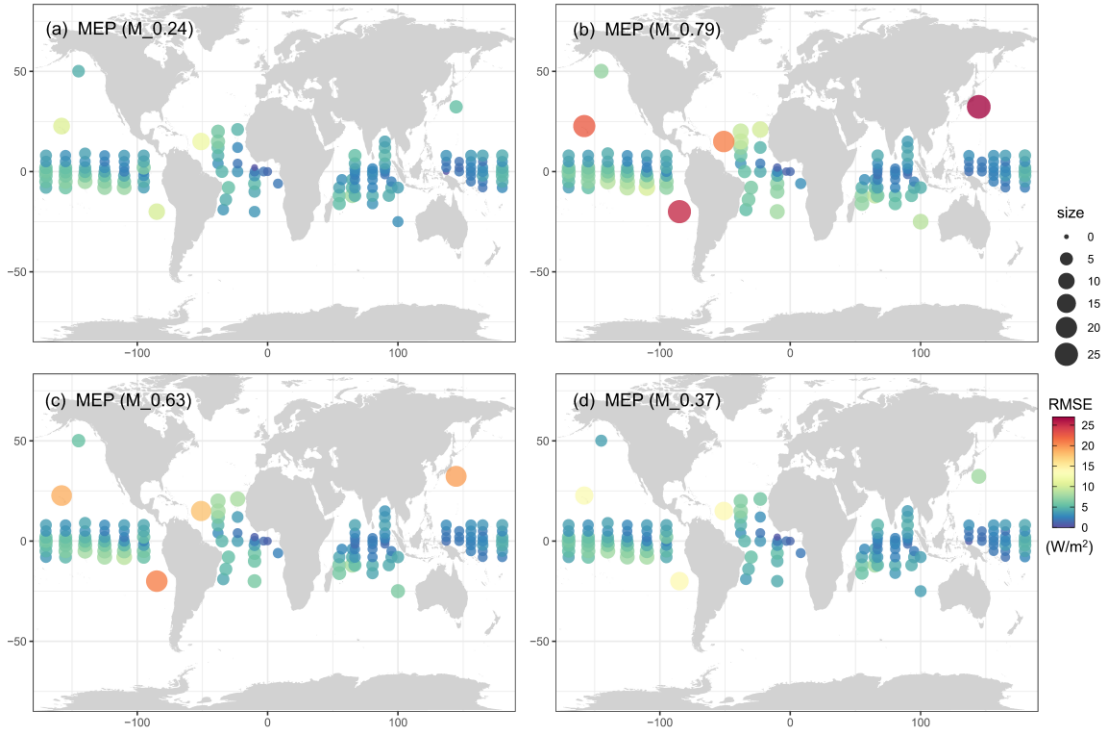
390   **Figure 2.** Spatial distribution of RMSE values in the comparison between latent heat flux estimated by the
391   improved MEP method (modified by four different Bowen ratio formulas) and buoy observations from 129
392   stations.

393

394
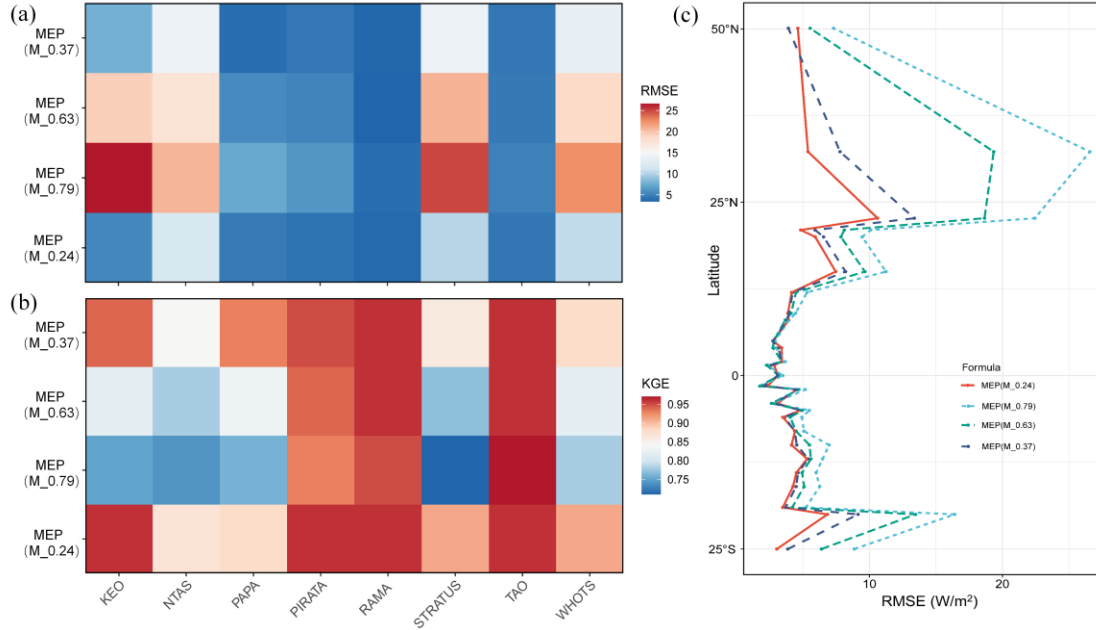
Figure 3. Comparisons between latent heat flux estimated by the improved MEP method using four empirical
Bowen ratio formulas and the buoy observations from each buoy array in term of RMSE (a) KGE value (b),
and latitudinal means of RMSE (c). Latitudinal means are based on data from 129 available buoy sites.

4.2 Dynamics of heat fluxes and Bowen ratio between original and improved MEP model

To thoroughly investigate the role of heat storage in the partitioning of surface energy and its implications

for the temporal dynamics of heat fluxes, we selected the KEO site for detailed analysis. This selection was

based on the site's long-term observational records and notable variability in flux patterns, which offered an

ideal context for a rigorous comparison of model-simulated error margins.

The improved MEP methods demonstrated comparable performance in estimating heat fluxes at the

KEO site when compared with other 128 sites (Fig. S3, Fig. 1), with the MEP (M_0.24) model exhibited the

most effective performance. Analysis of the time series data revealed significant variations in latent heat,

sensible heat, and Bowen ratio (Fig. 4). In the original MEP theory, the estimated LE exhibited an opposite

variation cycle (peak versus trough) compared to the observations. For instance, over a yearly period, the

observed peak in LE occurred in January 2005 (269 W·m^{-2}) and the trough in June 2005 (6.9 W·m^{-2}). In

contrast, the MEP simulated the peak in LE to occur in August 2005 (105 W·m^{-2}) and the trough in December

2004 (0.7 W·m^{-2}), resulting in a phase difference of 7 months for the peak and 6 months for the trough values.

Sensible heat flux (Fig. 4b) showed similar phase differences: observed H peaked in January 2005 (79 W·m^{-}

413   ^{2}) and reached its minimum in June 2005 (-3 W·m^{-2}), whereas MEP simulated *H* to peak in August 2005 (46

414   W·m^{-2}) and reach its minimum in December 2004 (0.6 W·m^{-2}), consistent with the pattern observed for *LE*.

415   It was noteworthy that the original MEP model simulated variations in *LE* and *H* align with R_n (Fig. S4),

416   which was reasonable over land where the small *G* value can often be disregarded. However, over the ocean,

417   the observed variations in R_n and *LE* do not align in terms of their cycles. The maximum R_n occurred in June

418   2004 (329 W·m^{-2}) and the minimum occurred in December 2004 (142 W·m^{-2}), with a 6-month delay in

419   relation to the variations in *LE*. Specifically, the peak R_n corresponded to the trough of *LE*, and the trough R_n

420   corresponded to the peak of *LE*. This delay indicated that the heat storage effect delayed the peak of *LE* and

421   altered the seasonal variations of *LE* and *H*.

422

423
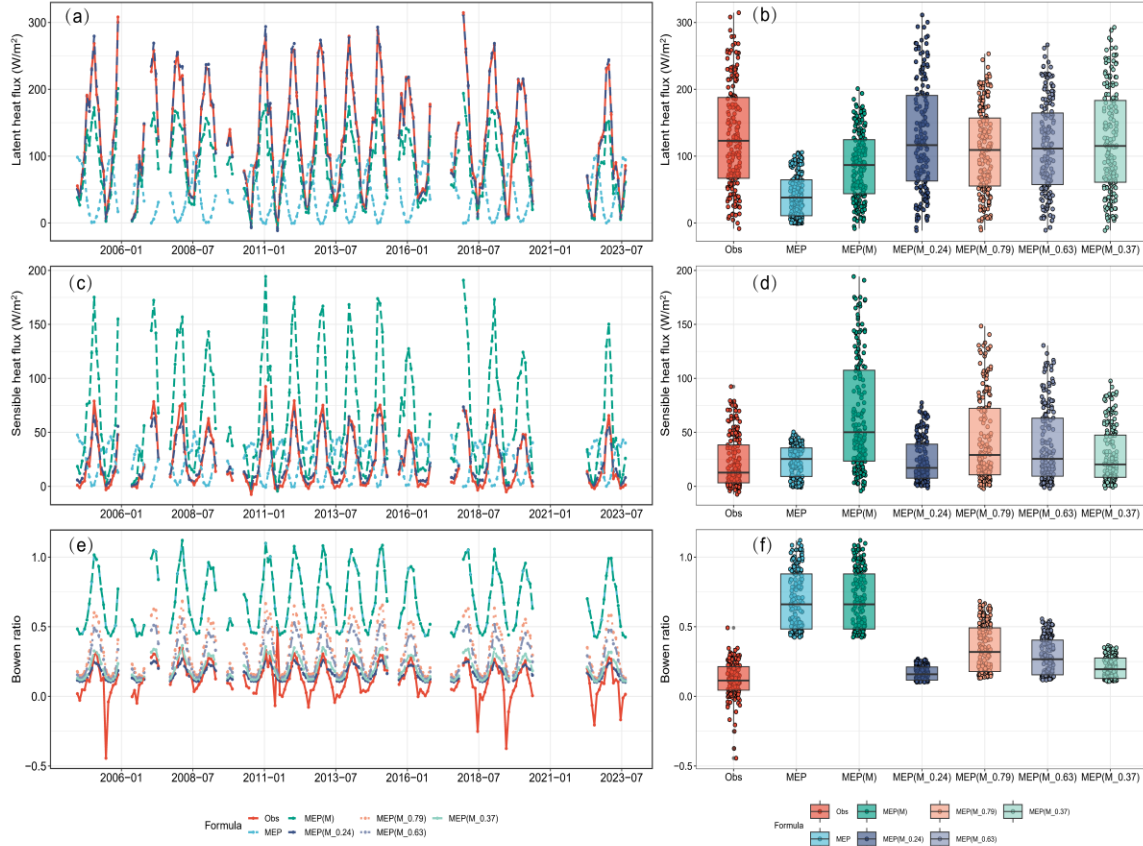
424   **Figure 4.** The inter-annual variations (a, c and e) and variabilities (b, d, and f) for latent heat flux, sensible
425   heat flux, and Bowen ratio at KEO site from June 17, 2004, to August 12, 2023. The fluxes in the comparison
426   include observations and the estimates from MEP using the original formula (MEP), the formula
427   incorporating the ocean heat storage (MEP(M)), and four other formula considering both ocean heat storage
428   and adjustment of Bowen ratio. Note that the (a) and (c) only display results using MEP *(M_0.24)* among all
429   four empirical Bowen ratio formulas for clearer comparison.
430

431   For the patterns of the Bowen ratio, both the original MEP formula and the modified formulas exhibited

432  consistent patterns with the observed values. The observed maximum Bowen ratio occurred in January 2005

433  (0.29) and the minimum in June 2005 (-0.4). However, the original MEP formula simulated a maximum of

434  1.01 and a minimum of 0.44, indicating a significant overestimation compared to the observed Bowen ratio.

435  This discrepancy suggested that on the ocean surface, the available energy (R_n-G) was predominantly

436  allocated to LE (Fig.S4). Among the four empirical formulas, $M\_0.24$ simulated LE, H, and Bowen ratio

437  values were closest to the observed values. The median of the observed Bowen ratio was 0.11, while the

438  original MEP Bowen ratio was 0.66. Among the four modified Bowen ratio formulas ($M\_0.24$, $M\_0.79$,

439  $M\_0.63$, $M\_0.37$), their median Bowen ratios were 0.15, 0.32, 0.27, and 0.19 respectively, with $M\_0.24$ being

440  the closest to the observed Bowen ratio.

441   Heat storage is crucial for the energy distribution process over the ocean surface. While the original

442  MEP formulas have been effectively validated when applied to surfaces with shallow depths such as water

443  and snow (Wang et al., 2014), they exhibit significant uncertainty when applied to the ocean surface. This

444  discrepancy primarily arises from the fact that land is a non-transparent medium with relatively small heat

445  storage values at monthly scales. Similarly, shallow water bodies also exhibit small heat storage values that

446  can often be ignored. In the study by Wang et al. (2014), for example, two lakes with depths of 2m (Lake

447  Tämnaren) and 4m (Lake Råksjö) still resulted in underestimated LE. However, for deeper lakes (generally >

448  3m depth), heat storage becomes significant and cannot be neglected (Zhao et al., 2016; Zhao & Gao, 2019).

449  On deep ocean surfaces, with the most recent average depth estimate of 3,682m from NOAA satellite

450  measurements, heat storage variations can influence depths up to 6,000m (Cheng et al., 2017). Therefore, the

451  impact of heat storage was substantial and cannot be disregarded. In the original MEP theory, heat storage

452  was not considered in the energy balance equation, where it was assumed that the net solar radiation (R_{ns}) is

453  absorbed by the ocean and $R_{nL}= LE + H + Q$. Then, the heat storage was obtained as $G = R_{ns} + Q$. In this

454  study, we compared the characteristics of MEP-derived G ($R_{ns} + Q$) with the observed G flux ($G = R_n - LE$

455  $- H$ (Fig. S5). MEP-derived G showed a good correlation ($R = 0.96$) and consistent trends with the observed

456  values (Fig. S5a & b), ranging from -4 to 81 W·m^{-2}. However, MEP-calculated Q (ranged from -210 to -65

457  W·m^{-2}) exhibited a negative correlation with the observed G (which ranged from -386 to 200 W·m^{-2}). Both

458  MEP-derived G and Q fluxes were significantly underestimated. Therefore, the prediction errors in LE and

459 *H* originated from the inability to accurately quantify the heat storage. Hence, considering the influence of

460 heat storage was crucial for accurately predicting *LE* and *H* over the ocean surface.

461 **4.3 Evaluation of global radiation and heat storage flux**

462 4.3.1 Evaluation of net radiation

463 After considering the effect of heat storage and the Bowen ratio, the improved MEP method demonstrated

464 its high performance at the site scale. The results suggested that improved MEP method held substantial

465 promise for further application at a global scale. To facilitate this, we assessed the primary input variables of

466 the improved MEP method (including R_n, G, and T_s) to identify datasets with the best accuracy.

467 Net radiation, as the primary variable in the energy balance equation, significantly influenced the

468 uncertainty of the MEP model (Huang et al., 2017). Selecting a reliable R_n product was essential for accurately

469 estimating global latent and sensible heat fluxes. Previous studies have evaluated the available global ocean

470 surface R_n datasets at daily scales using observations from 68 moored buoy sites (Liang et al., 2022). In this

471 study, we conducted a comprehensive evaluation of current available monthly R_n products, including three

472 remote sensing-based products (CERES4, GEWEX-SRB, and JOFURO3) and two atmosphere reanalysis-

473 based products (ERA5 and MERRA2) at 129 buoy sites. All products exhibited good consistency with buoy

474 observations (Table 3 and Fig. S6), with R^2 values greater than 0.78. In terms of RMSE, the error rankings

475 for all products were as: J-OFURO3 (10 W·m^{-2}) < ERA5 (39.03 W·m^{-2}) < CERES4 (40.67 W·m^{-2}) <

476 GEWEX-SRB (41.83 W·m^{-2}) < MERRA2 (49.23 W·m^{-2}). It was evident that J-OFURO3 demonstrated the

477 highest accuracy, as indicated by RMSE, NSE, and KGE statistics. This result was also consistent with

478 previous assessments of global R_n (Liang et al., 2022), emphasizing J-OFURO3 as the least erroneous among

479 all individual products and superior to existing alternatives including CERES4, ERA5, MERRA2, GEWEX-

480 SRB, JRA55, OAFlux, and TropFlux.

481 **Table 3.** Evaluation of global monthly net radiation products against buoy observations

Products	R^2	ME (W·m^{-2})	MAE (W·m^{-2})	RMSE (W·m^{-2})	PBIAS (%)	NSE	KGE
J-OFURO3	**0.96**	**1.6**	**7.3**	**10.0**	**1.0**	**0.96**	**0.97**
ERA5	0.79	28.8	30.3	39.0	17.8	0.45	0.77
MERRA2	0.78	39.7	41.2	49.2	24.8	0.15	0.68
CERES4	0.81	31.4	32.6	40.6	19.6	0.42	0.76
GEWEX-SRB	0.78	32.6	33.8	41.8	20.2	0.37	0.76

4.3.2 Evaluation of heat storage

The study underscored the importance of considering heat storage in simulating heat fluxes using the improved MEP model. For the first time, we assessed global heat storage using the J-OFURO3, ERA5, MERRA2, and ΔOHC datasets. In addition to assessing these individual datasets, we investigated the potential for enhancing accuracy through data fusion methods. We employed the BTCH and AA method to fuse heat storage data and compared the accuracy between individual datasets and fused datasets (Table 4). The results revealed that while using the AA method (e.g., AA4) to fuse yields smaller errors compared to ERA5, MERRA2, and ΔOHC, it still failed to achieve the accuracy of the J-OFURO3 product. Similarly, the BTCH method, despite fusing data from three or four sources, also does not match the accuracy of the J-OFURO3 method, as indicated by metrics of R^2, RMSE, and KGE. The heat storage derived from J-OFURO3 data showed high consistency with observations (R^2=0.95), as illustrated in Fig. 5 (spatial distribution of errors depicted in Fig.S7). Therefore, this study employed the heat storage data derived from the J-OFURO3 dataset as the input for the MEP model.

To ensure consistency with radiation data source, the Sea Surface Temperature (*SST*) data from J-OFURO3 was utilized for T_s inputs, which was derived as the ensemble median from 12 global *SST* products (Tomita et al., 2019). Ultimately, the input variables including net radiation, heat storage, and sea surface temperature for driving MEP model were all determined from the J-OFURO3 dataset spanning from 1988 to 2017. Saturated specific humidity was computed as a function of *SST* and surface air pressure (from ERA5) using the Clausius-Clapeyron equation. The reliability of gridded data for the variables R_n, G, and T_s were simultaneously examined at an observational site (Fig.S8), where all three variables demonstrated high consistency with observed data from August 2004 to December 2017 (with $R^2 > 0.96$), effectively capturing the monthly dynamics of R_n, G, and T_s.

Table 4. Assessment of monthly heat storage between global remote sensing datasets and buoy observations

Products	R^2	ME (W·m^{-2})	MAE (W·m^{-2})	RMSE (W·m^{-2})	PBIAS (%)	NSE	KGE
J-OFURO3	**0.95**	**-3.5**	**15.3**	**19.7**	**-7.4**	**0.94**	**0.91**
ERA5	0.88	7.0	25.1	33.2	14.8	0.84	0.80

MERRA2	0.86	11.6	27.1	36.1	24.5	0.81	0.72
OHC	0.35	-48.2	64.4	86.9	-101.9	-0.11	-0.10
BTCH3-1 (E M J)	0.89	7.1	22.8	30.5	15.1	0.86	0.81
BTCH3-2 (E M O)	0.88	4.6	24.0	31.4	9.9	0.85	0.86
BTCH4	0.91	5.9	19.7	26.2	12.5	0.90	0.86
AA2(EM)	0.87	9.3	25.4	34.1	19.7	0.83	0.76
AA3 (EMJ)	0.91	4.7	20.2	26.7	10.1	0.90	0.87
AA4 (E M J O)	0.91	11.5	21.4	28.6	24.4	0.88	0.74

Note: BTCH3-1 represents the fusion of three products (ERA5, MERRA2, and J-OFURO3) using the BTCH method; TCH3-2 represents the fusion of ERA5, MERRA2, and OHC; BTCH4 represents the fusion of ERA5, J-OFURO3, MERRA, and OHC. AA denotes the Simple Arithmetic Average (AA) method. The evaluation period spans from 1988 to 2017, and the best-performed statistics are indicated in bold type.
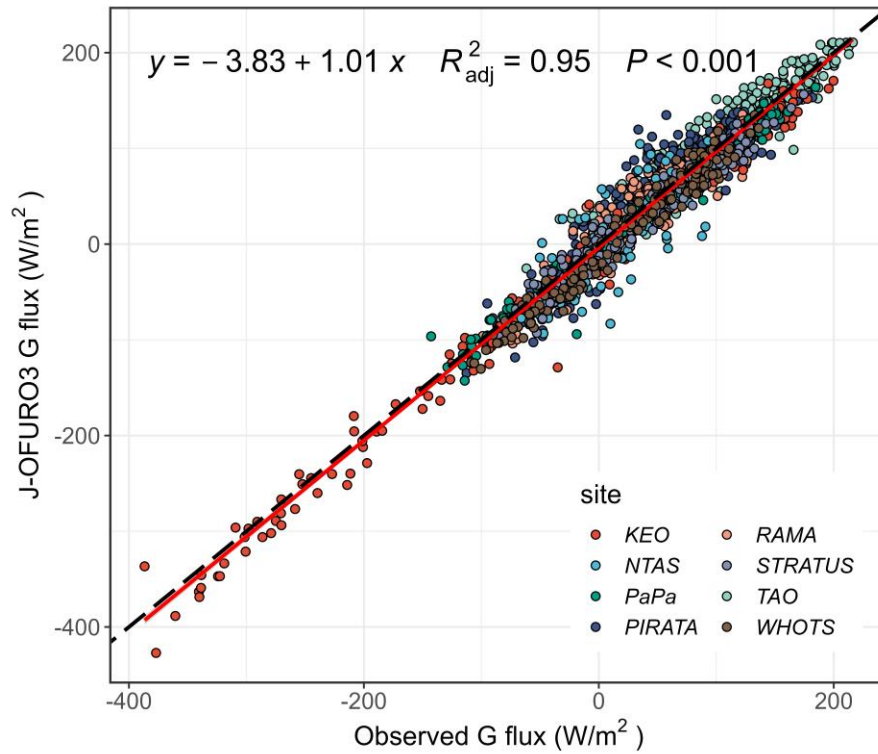
Figure 5. Assessment of heat storage (G) flux derived from remote sensed J-OFURO3 dataset against buoy observations. Distinct colors represent data collected from different buoy arrays.

4.4 Estimating long-term global ocean surface heat fluxes by improved MEP model

4.4.1 New estimate of global latent and sensible heat fluxes

After identifying the optimal driving dataset, this study employed the best-performed improved MEP method

(i, e., *M_0.24*, hereinafter referred to as MEP for simplicity, while the original MEP formula was denoted as

522   *MEP (ori)* for global scale estimation, producing new estimations of latent and sensible heat fluxes for the

523   period 1988-2017 (Table 5). The MEP model calculated the multi-year average *LE* as 92.87 W·m^{-2} and the

524   sensible heat flux as 12.27 W·m^{-2} from 1988 to 2017. In comparison, *LE* ranged from 88.95 (OAFlux) to

525   100.54 W·m^{-2} (MERRA2), and *H* ranged from 10.17 (J-OFURO3) to 13.16 W·m^{-2} (MERRA2) for the other

526   four products. The original MEP method yielded estimates of *LE* as 52.70 W·m^{-2} and *H* as 25.07 W·m^{-2},

527   significantly underestimating *LE* and overestimating *H* compared to estimates from other products. As

528   previously demonstrated (Sections 4.1 & 4.2), the original MEP method overestimated *G* (42.20 W·m^{-2}) and

529   exhibited notable deviations in the Bowen ratio. Therefore, the improved MEP method provided a more

530   reasonable global estimation of *LE* and *H*.

531   Regarding the global spatial pattern (Fig.6), the MEP-derived latent heat exhibited higher values in low-

532   latitude regions but significantly decreased beyond 45° latitude. The highest *LE* values were observed in the

533   southern Indian Ocean near Australia, the Pacific and Atlantic regions near South America, and the Indian

534   Ocean near southern Africa. The peak values were observed within western boundary current systems (ranged

535   from 200 to 260 W·m^{-2}), including the Gulf Stream in the North Atlantic and the Kuroshio in the western

536   North Pacific. Impacted by the variations in oceanic currents near the equator, two general areas of higher

537   *LE* have emerged (Yu et al., 2011), leading to notably low *LE* at the equator (88 W·m^{-2}), peaking at ~18°S at

538   132 W·m^{-2} (Fig. 6 & Fig. 7). The MEP estimated *LE* exhibited a similar spatial pattern with other four

539   products globally (Fig.6), particularly resembling OAFlux between 15°S and 15°N (Fig. 7). Overall, for the

540   region between 30°S and 30°N, the *LE* values were ranked as follows: OAFlux < MEP < J-OFURO3 < ERA5

541   < MERRA2, which was consistent with the magnitude of available energy. For sensible heat, MEP-derived

542   H closely resembled that of ERA5 and MERRA2, with higher values predominantly occurred in two western

543   boundary current systems, the South Indian Ocean near Australia area, and the Arctic Ocean. The improved

544   MEP method mitigated the issue of overestimating *H* in mid-to-high latitudes compared to its original form

545   (Fig.6l), resulting in a more realistic spatial pattern. In high latitudes, J-OFURO3 exhibited higher H values

546   than MEP and other comparable products in the Northern Hemisphere, with negative values observed

547   between 45°S and 55°S. MEP generally estimated *H* within an intermediate range compared to other products,

548   displaying a distribution that was more reasonable than that of J-OFURO3 product.

549

Table 5. Global area-averaged multi-annual mean estimates of latent heat flux

LE products	LE (W·m⁻²)	Evaporation (mm/yr)	H (W·m⁻²)	G (W·m⁻²)
MEP (0.24)	92.8	1195.5	12.2	19.7
ERA5	99.2	1277.8	12.0	34.2
MERRA2	100.5	1294.3	13.2	35.5
J-OFURO3	94.9	1222.2	10.1	19.7
OAflux	88.9	1145.1	10.4	/
MEP (ori)	52.7	678.5	25.1	42.2

551 Note: The period spans from 1988 to 2017. The MEP (0.24) denotes the improved MEP model, while MEP
552 (ori) represents the original MEP model.
553

554
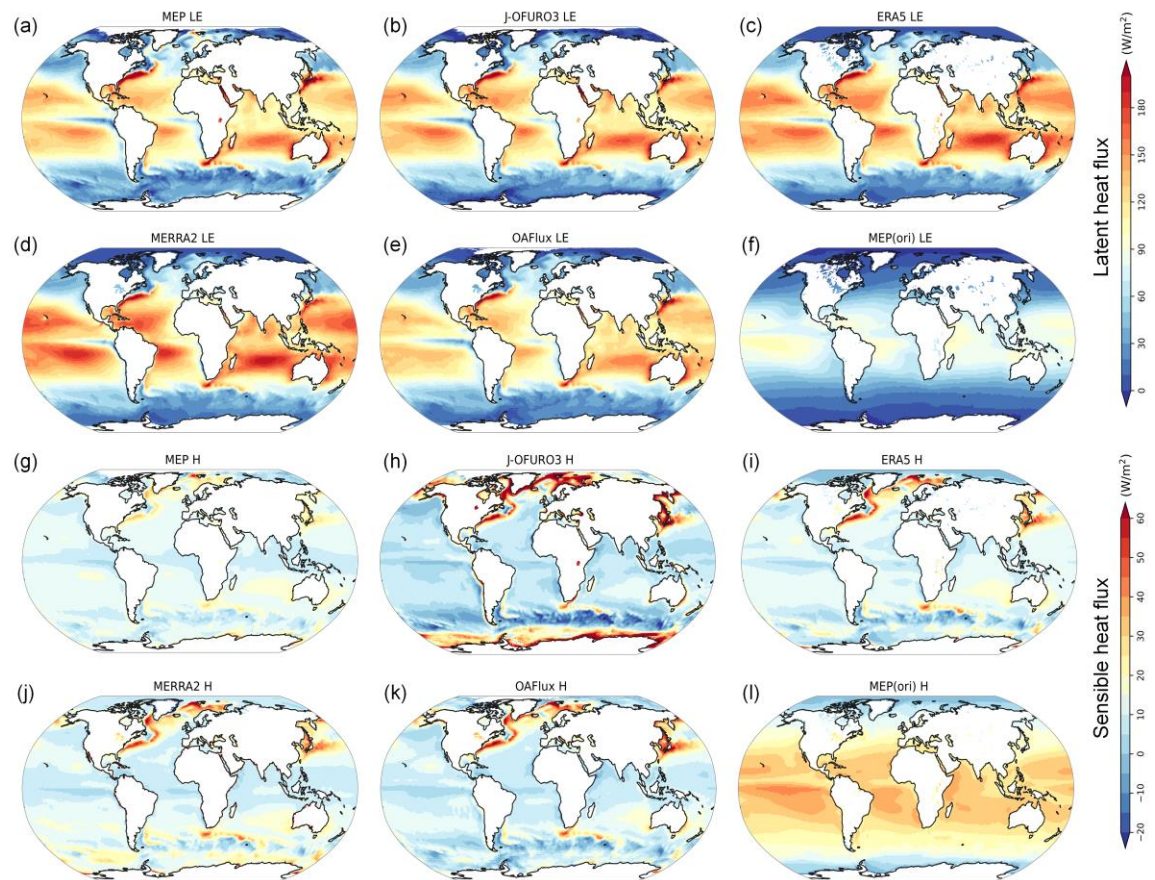
555 **Figure 6.** Global spatial maps of annual mean latent heat flux (*LE*) and sensible heat flux (*H*) during 1988-
556 2017. Panels (a)-(f) depict latent heat flux derived from the improved MEP method, J-OFURO3, ERA5,

557 MERRA2, OAFlux, and the original MEP method. Panels (g)-(l) show sensible heat flux from the same
558 datasets.
559

560
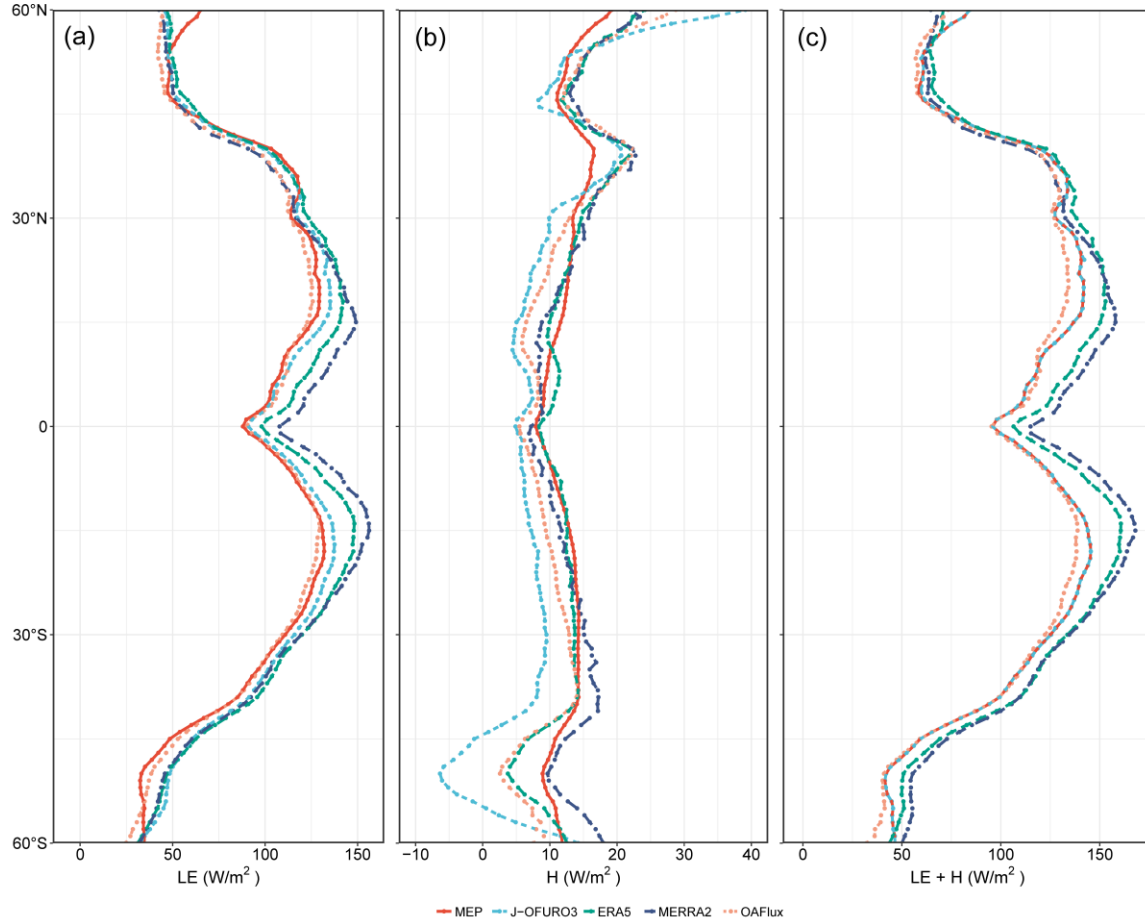
Figure 7. Meridional profiles of latent heat (left panel), sensible heat (middle panel) and their sum
representing available energy (right panel) for the period 1988-2017, produced by MEP, J-OFURO3, ERA5,
MERRA2, and OAFlux datasets.

4.4.2 Validation of global latent heat products against the observational sites

To evaluate the discrepancies between MEP estimated *LE* and other datasets, this study validated global-scale *LE* at 129 observational sites (as depicted in Fig.8 & Table 6). MEP-estimated *LE* showed strong consistency with buoy observations, achieving an R^2 of 0.79, a ME of 1.26 W·m^{-2}, and RMSE of 16 W·m^{-2}, all surpassing those of alternative products, underscoring its superior performance. Moreover, the MEP method exhibited superior performance with a higher NSE value of 0.77 and KGE of 0.89, demonstrating enhanced accuracy, reliability, and robustness. According to the RMSE evaluation criterion, the ranking of best-performed *LE* products was as: MEP, J-OFURO3, OAFlux, ERA5, MERRA2. In a recent comprehensive assessment of 15 global ocean *LE* products (Tang et al., 2023), RMSE values ranged from

574 17.2 to 45.3 W·m⁻², in which J-OFURO3 emerged as the best-performing product with the lowest RMSE of

575 17.2 W·m⁻², highest correlation coefficient (R) of 0.89, and ME of 6.5 W·m⁻². Studies have also shown

576 minimal bias were given by J-OFURO3 on daily scale (Bentamy et al., 2017). This superior performance of

577 J-OFURO3 dataset can be attributed to the use of continuously updated bulk algorithms (COARE 3.0 version),

578 the ongoing optimization of near-surface parameters (Tomita & Kubota, 2018), as well as the improved

579 spatial resolution (0.25°). In this study, the improved MEP estimation of *LE* outperformed that of J-OFURO3,

580 demonstrating higher accuracy and lower error (ME=1.26 W·m⁻²), thereby establishing it as the most accurate

581 global *LE* product currently available.

582
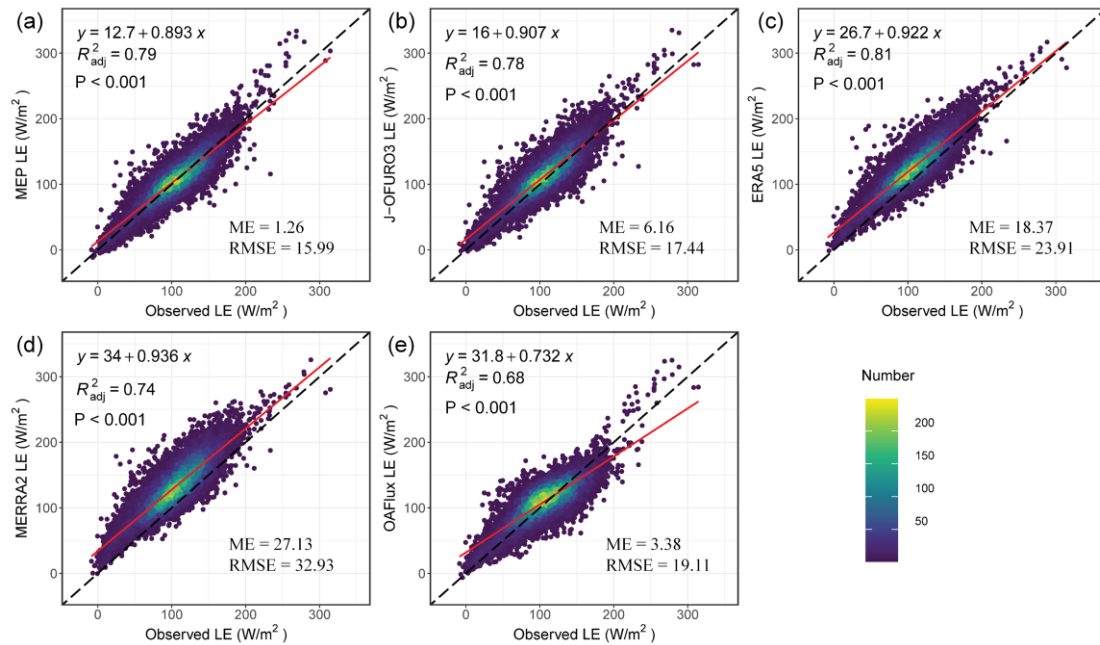
583 **Figure 8.** Scatter density plots of latent heat flux taken from different products versus observations from 129
584 buoy stations during the period 1988-2017: (a) Improved MEP model, (b) J-OFURO3, (c) ERA5, (d)
585 MERRA2, and (e) OAFlux. A total of 15444 records of latent heat observations are included.
586

587 **Table 6.** Evaluation of latent heat flux from different methods against buoy observations

Products	R^2	ME (W·m⁻²)	MAE (W·m⁻²)	RMSE (W·m⁻²)	PBIAS (%)	NSE	KGE
MEP	0.79	**1.3**	**12.2**	**15.9**	**1.2**	**0.77**	**0.89**
J-OFURO3	0.78	6.3	13.4	17.4	5.8	0.73	0.87
ERA5	**0.81**	18.4	19.9	23.9	17.3	0.48	0.80
MERRA2	0.74	27.1	28.1	32.9	25.5	0.02	0.70
OAFlux	0.68	3.4	14.9	19.1	3.2	0.67	0.79

588 Note: The evaluation period spans from 1988 to 2017, and the best-performed statistics are indicated in bold
589 type.

 ### 4.4.3 Comparisons of Bowen ratios

591 The improved MEP model achieved accurate *LE* estimation after refining the process of partitioning the

592 surface energy budget, specifically through revisions to the Bowen ratio. The improved MEP method notably

593 decreased the global-scale Bowen ratio, as illustrated in Fig. 9 and 10. Regarding latitude averages, the

594 Bowen ratio of the original MEP formula ranged from 0.37 to 1.48 (with a median of 0.80), whereas the

595 modified MEP Bowen ratio ranged from 0.09 to 0.35 (median of 0.18). Specifically, in the low-latitude region

596 (10°S-10°N), the Bowen ratio of the modified MEP formula decreased from 0.37 to approximately 0.1,

597 aligning closely with the Bowen ratios obtained from other reanalysis products (MERRA2, ERA5, OAFlux,

598 and J-OFURO3). Globally, the median Bowen ratios of the products were as follows: MERRA2 (0.15), MEP

599 (0.12), ERA5 (0.09), OAFlux (0.08), and J-OFURO3 (0.06). Spatially, the MEP Bowen ratio resembled

600 ERA5 in mid to low latitudes but exhibited deviations from other products at high latitudes, where those

601 products showed fluctuating changes in the Bowen ratio (Fig.10). For instance, other products displayed

602 abrupt transitions from negative to positive Bowen ratios in the Arctic and Antarctic regions, whereas MEP-

603 derived values demonstrated greater stability in variations at higher latitudes. This discrepancy was likely

604 due to the reanalysis products relying on the bulk method, which was sensitive to variations in wind speed

605 and temperature gradients, leading to errors in simulating high wind speeds at the poles and causing

606 fluctuations in latent and sensible heat. In contrast, the MEP model strictly adheres to energy conservation

607 principles and operates independently of wind speed and temperature gradients, resulting in a more accurate

608 estimate of the Bowen ratio. For example (Fig.S9), at the high-latitude PAPA buoy site (144.9°W, 50.1°N),

609 the Bowen ratio estimated by MEP (median 0.24) closely matched the observed Bowen ratio (median 0.23).

610 In contrast, all the other products underestimated the Bowen ratio, with J-OFURO3 (median -0.09) and

611 OAFlux frequently exhibiting negative values. The Bowen ratio derived from MEP fit well with a

612 Generalized Additive Model (GAM) (Fig.9). The implicit functional relationship between Bowen ratio and

613 latitude was expressed as ($R^2 = 0.996$, $p < 0.001$): $B_{oa}(lat) = 0.207218 + f(lat) + \varepsilon$, where *f(lat)* represents a

614 smoothing function derived from a smooth curve, and ε denotes the error term. However, the specific

615 functional form of *f(lat)* cannot be explicitly determined. Therefore, a polynomial regression method was

616 employed to explicitly fit B_{oa} and *lat*, resulting in ($R^2 = 0.91$, $p < 0.001$): $B_{oa} = 9.97 \times 10^{-2} - 3.45 \times 10^{-4} \times lat$

617      $+ 4.71 \times 10^{-5} \times lat^2 + \varepsilon$ (as in Fig.S10). This equation can serve as a reference for partitioning surface energy

618   in data-sparse oceanic regions.

619
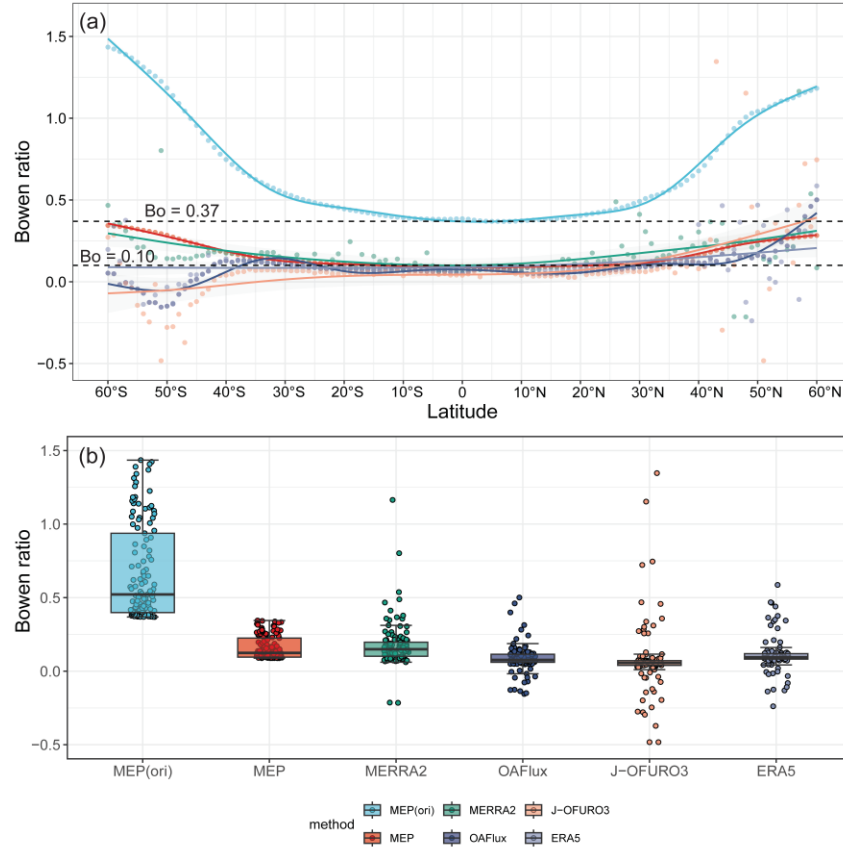
620 **Figure 9.** Global ocean latitudinal averaged Bowen ratio derived by the MEP method and four other products
621 from 1988 to 2017. (a) Latitudinal averaged Bowen ratio derived from the MEP model using original and
622 modified Bowen ratio formulas, with points fitted by a generalized additive model (GAM). (b) Statistical
623 distribution of the latitudinal annual mean Bowen ratio.

624

625
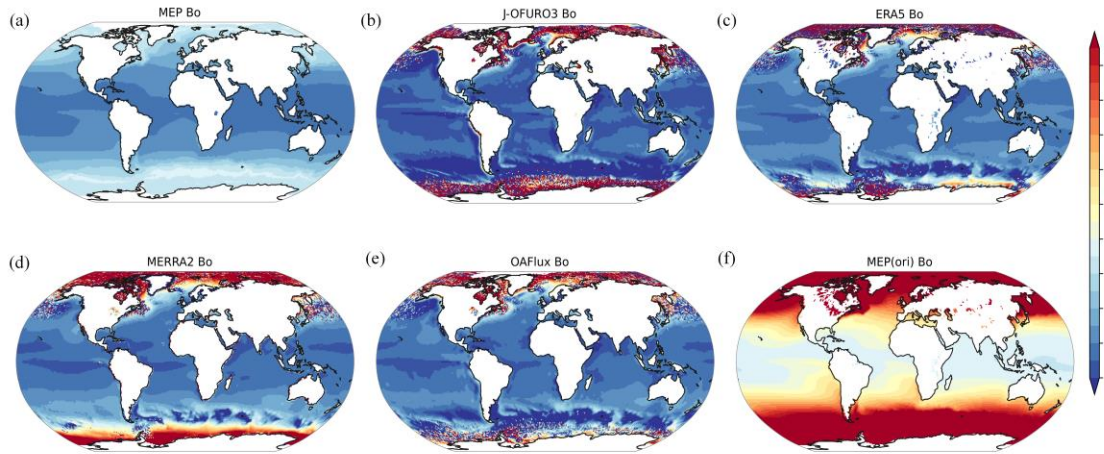
626 **Figure 10.** Global distribution of ocean annual mean Bowen ratio during 1988-2017: (a) Improved MEP
627 method, (b) J-OFURO3, (c) ERA5, (d) MERRA2, (e) OAFlux, and (f) MEP original method.

4.5 Spatial-temporal variability of ocean evaporation

Heat flux reflects the energy exchange between the ocean and the atmosphere, while evaporation (*ET*) reflects moisture exchange within the water cycle. The spatiotemporal patterns of evaporation were analyzed using the Sen's slope and Mann-Kendall test methods (Fig. 11). For the global ocean, approximately 74% of the regions showed an increasing trend, with about 27% of the grids exhibiting statistically significant increases ($p < 0.05$). In contrast, 26% displayed a decreasing trend, with only 5% of the grids showing statistically significant decrease ($p < 0.05$). For the whole periods, the regions with the highest increasing trends were predominantly observed near western boundary current systems, the convergence zones of the East Australian Current and the South Equatorial Current, and the convergence zones of the Eastern South Equatorial Current and the Brazil Current along South America. Decreasing trends were primarily observed in equatorial regions of the Pacific and Atlantic Oceans, as well as near the Labrador and Kuroshio currents and north of the Antarctic Circle. It was indicated that regions with significant increases (decreases) in evaporation generally correspond closely to the distribution of major warm currents (cold currents) spatially. However, global ocean evaporation experienced a notable shift around 2003, as illustrated in Figs.11b and 11c. The downward trend observed from 2003 to 2017 counteracted a significant portion of the growth trend that occurred during the previous 16 years (1988-2003), particularly evident in the mid-latitude regions (15ºS-20ºN). In the middle-to-low latitudes (0º-30ºN), nearly all ocean grids exhibited opposite trends around 2003. Spatially, regions that displayed the largest increasing trends during 1988-2003 transitioned to show the most substantial decreasing trends between 2003 and 2017. This includes regions associated with western boundary current systems, convergence zones of the East Australian Current and the South Equatorial Current, as well as equatorial regions of the Pacific and Atlantic Oceans (Fig. 11c). To further investigate the shift in ocean evaporation after 2003, we analyzed the interannual variability of global annual mean area-weighted evaporation using all available datasets (as shown in Fig.12).

Over the multi-year period from 1988 and 2017, MEP, J-OFURO3, ERA5, and MERRA2 all exhibited significant increasing trends in *ET*. MEP estimated an evaporation increase rate of 2.31 mm/year, whereas OAFlux showed a non-significant trend (Fig. 12). While different datasets revealed varying magnitudes of evaporation changes, most exhibited a similar temporal pattern: an increasing trend from 1988 to around 2003, followed by a hiatus during 2003-2010, and ultimately a decreasing trend after 2010 (Fig. 12a).

656 Specifically, MEP indicated an increasing trend in evaporation of 3.58 mm/year from 1988 to 2010, followed

657 by a decrease of 2.18 mm/year after 2010 (Fig. 12a). The slowdown and transition of evaporation during

658 2003-2010 aligned with the concept of a "global warming hiatus" (Medhaug et al., 2017; Sung et al., 2023),

659 referring to the period when global mean surface air temperatures did not continue to rise between 1988 and

660 2012. Previous studies have proposed four potential explanations for this global warming hiatus: internal

661 variability, external drivers, the Earth's response to CO_2, and radiative forcing (Medhaug et al., 2017). This

662 study indicates that changes in radiative forcing (Fig. 12b) can significantly affect the interannual variability

663 of evaporation (Fig. 12a) and surface temperature (Fig. 12c). This finding is consistent with previous research

664 that attributed more than 50% of the uncertainty in MEP-modeled fluxes to the radiation term (Huang et al.,

665 2017). Although surface temperature began to increase after 2012, the decrease in available energy remained

666 the primary driver behind the decline in evaporation.

667
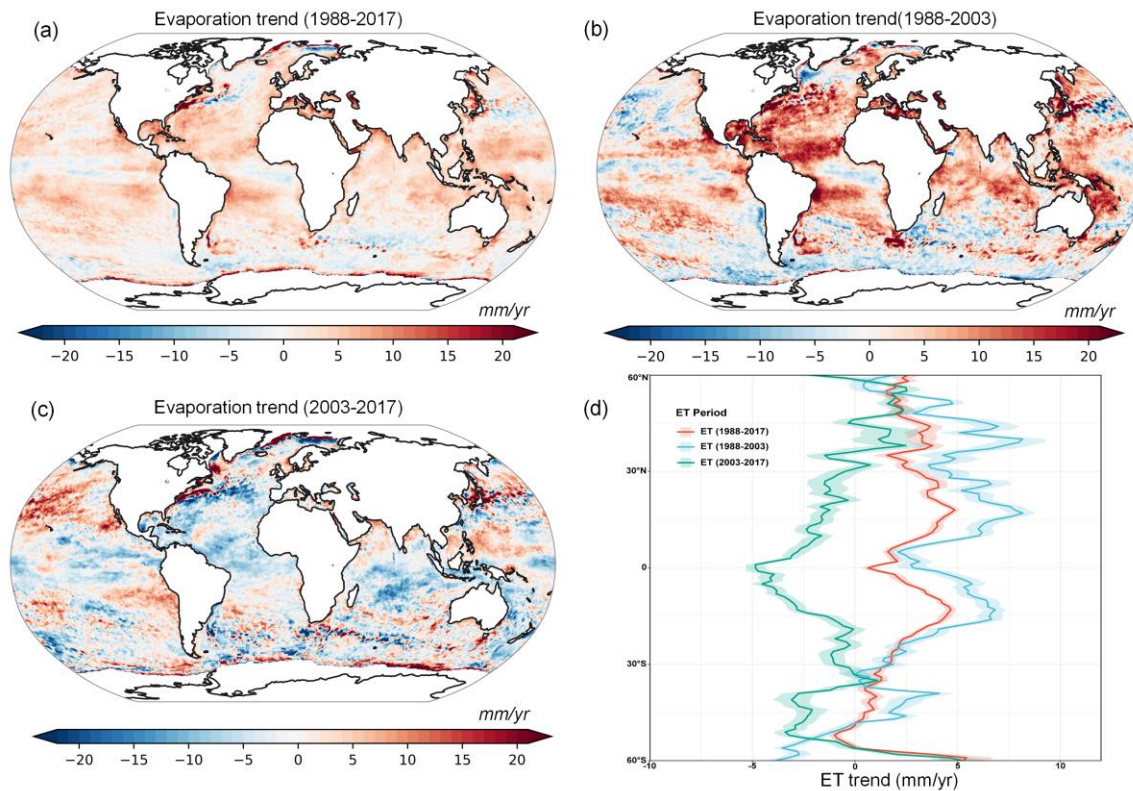
669 **Figure 11.** Spatial distribution of multi-year trends in ocean evaporation estimated by the improved MEP
670 method during (a) the period 1988-2017, (b) the period 1988-2003, (c) the period 2003-2017, and (d) the
671 latitudinal average changes across three different periods.

672
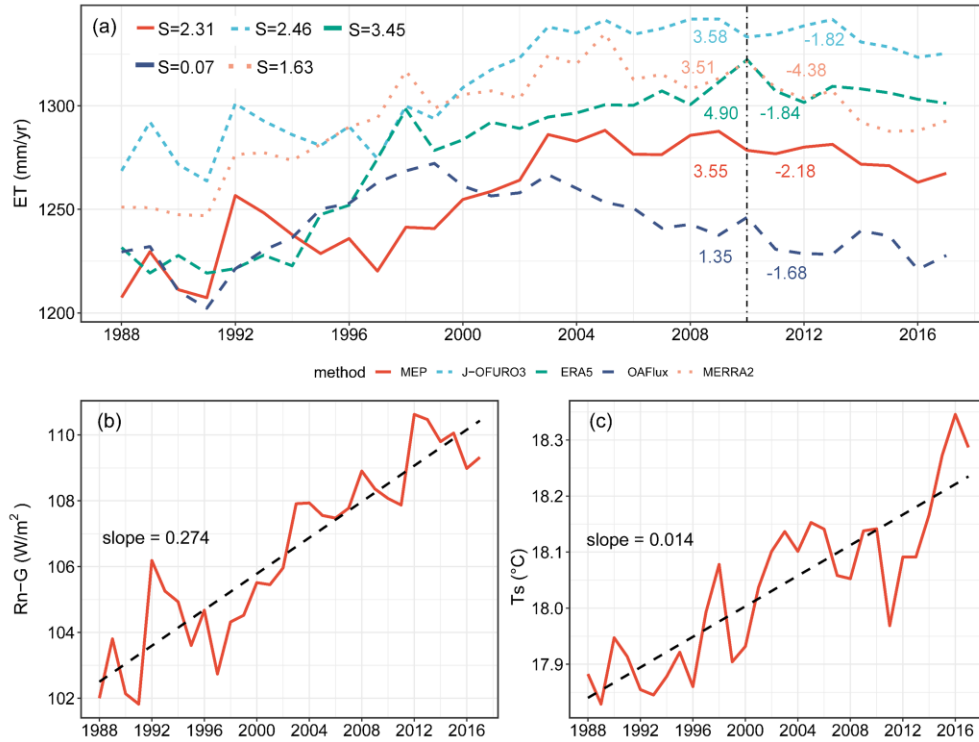
Figure 12. Time series of area-averaged multi-annual mean evaporation from the improved MEP method (a), available energy (b), and sea surface temperature (c) over the global oceans during 1988-2017. The black dotted line in panel (a) marks the year 2010, and the label "S = 2.31" indicates that the MEP-estimated global multi-annual mean evaporation increased at a rate of 2.31 mm/year during 1988-2017, with change rates of different ET datasets represented by various colors. The black dashed lines in panels (b) and (c) denote the linear regression lines.

5. Discussion

5.1 Quantifying the impact of heat storage and radiation with sensitivity analysis

The sensitivity analysis revealed the significant influence of input variables on latent heat flux derived from the MEP model. Notably, the heat storage (G) exhibited seasonal variations with both positive and negative values (Fig. 13). Positive G values coincided predominantly with summer in the Northern Hemisphere (winter in the Southern Hemisphere), specifically from June to August (Fig. 4 and Fig. S5). During this season, intensified solar radiation enhances the net energy input (R_n) at the ocean surface, leading to heat absorption and retention. Consequently, the energy available (R_n - G) for evaporation diminishes. The analysis indicated that R_n significantly influenced the energy-driven evaporation process, with a sensitivity coefficient exceeding 1 (median 1.74), highlighting its pivotal role. In contrast, G negatively impacted evaporation, as indicated by a sensitivity coefficient of -0.74. Specific humidity (median 0.08) and sea surface

690 temperature had relatively minor effects, consistent with previous MEP model findings focused on terrestrial

691 surfaces (Isabelle et al., 2021).

692   Conversely, negative values of heat storage predominate during winter, particularly from December to

693 February in the Northern Hemisphere (June to August in the Southern Hemisphere). Despite reduced solar

694 radiation during this period, residual heat stored from summer gradually releases into the atmosphere,

695 resulting in greater energy output than input. This surplus energy increases the available energy for

696 evaporation, leading to a positive sensitivity coefficient for G (median 0.29), second only to R_n (median 0.71).

697 Consequently, this process generally reduces sea surface temperature, resulting in a negative sensitivity

698 coefficient for surface temperature. Overall, these findings underscored the significant influence of R_n on

699 latent heat flux, with G ranking as the second most influential variable in MEP estimates over ocean surfaces.

700 For instance, a 10% decrease in positive G yielded a 7.4% increase in evaporation, while a 10% increase in

701 negative G resulted in a 2.9% increase in evaporation, assuming other variables remain constant. Thus, R_n

702 and G emerged as two primary drivers of oceanic evaporation, with humidity and temperature exerting

703 minimal influence.

704   The accuracy of available energy estimates significantly LE simulations, as it serves as the direct energy

705 source for partitioning latent and sensible heat fluxes. Although the bulk methods (e.g., COARE 3.0

706 algorithms) used for estimating heat fluxes are independent of surface energy budget allocation, discrepancies

707 in LE estimation still correlate strongly with validated biases against observations in available energy

708 estimates (see Tables 3 and 4). Notably, the MERRA2 product exhibited higher errors in simulating R_n and

709 G compared to observations, leading to significant biases in LE estimation. In contrast, the ERA5 product

710 demonstrated superior performance in simulating R_n and G, thereby achieving higher accuracy in LE

711 estimation. Consequently, the energy-balance-based MEP model excels in accurately estimating surface heat

712 fluxes by directly reflecting energy allocation. Unlike bulk methods, the MEP approach reduces sensitivity

713 to temperature and humidity gradients, thereby minimizing uncertainties in LE simulations (Pelletier et al.,

714 2018). This advancement enhances the MEP model's utility in global energy and water cycle research,

715 particularly pertinent for future climate change studies.

716

717
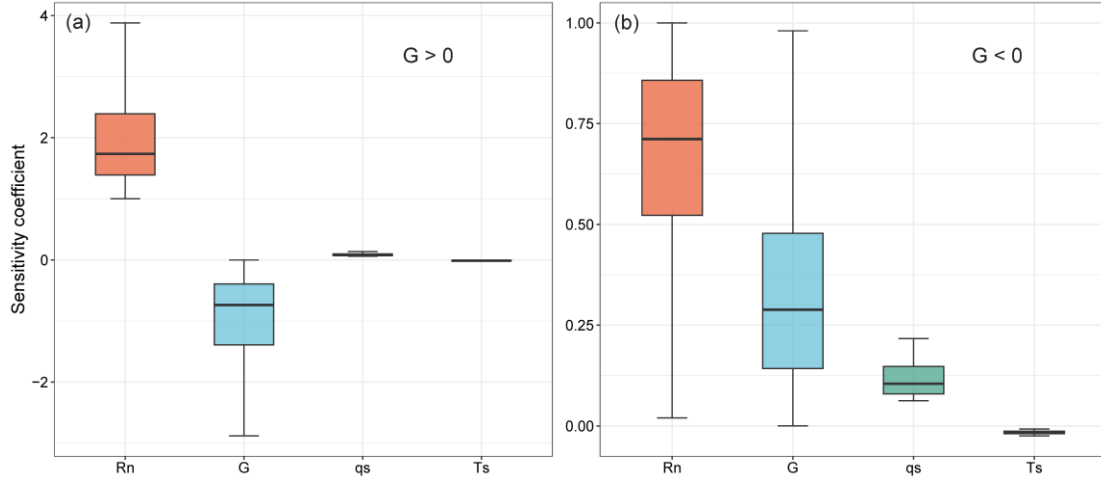
718 **Figure 13.** Sensitivity coefficient associated with inputs variables for the improved MEP method at all 129
719 buoy stations: (a) for positive G values, and (b) for negative G values.
720

721 **5.2 Discrepancy of empirical Bowen ratio formulas**

722 B_o plays a crucial role in understanding the surface energy partitioning process. In this study, four empirical

723 formulas were utilized to modify the MEP model and evaluated against the observed LE, each with distinct

724 conditions of applicability and suitability for integration with the MEP model: (1) $B_{oa}=0.63B_o{}^*-0.15$ was

725 derived from direct observational data fitting (Hicks and Hess, 1977). This formula was applicable for surface

726 temperatures above 16°C, particularly within latitudes between 40°N and 40°S, making it more suitable for

727 lower latitude regions; (2) $B_{oa}=0.79B_o{}^*-0.21$ was derived using the Priestley–Taylor model under advection-

728 free conditions (Priestley and Taylor, 1972). The coefficients were determined based on a mean α value of

729 1.26, although this value can vary in practice. Recent studies have revealed significant discrepancies due to

730 the neglect of interaction between variations in R_n and T_s (Yang & Roderick, 2019). To address this limitation,

731 the equation (3) $B_{oa}=0.24B_o{}^*$ was developed based on the maximum evaporation theory, considering the

732 feedback mechanisms between R_n and T_s while assuming that G is small or negligible. The empirical

733 coefficient 0.24 was determined by fitting B and T_s across the global ocean surface (Yang & Roderick, 2019);

734 and (4) $B_{oa}=0.37B_o{}^*-0.05$ was formulated based on principles derived from atmospheric boundary layer (ABL)

735 theory (Liu & Yang, 2021), with coefficients also fitted from relationships between B_{oa} and T_s. It should be

736 noted that the derivations of $B_{oa}=0.24B_o{}^*$ and $B_{oa}=0.37B_o{}^*-0.05$ were based on fitting using LE from the

737 OAFlux dataset rather than direct buoy observations. Overall, the MEP model incorporated with $B_{oa}=0.24B_o{}^*$,

738 exhibited superior accuracy at both localized and global scales, effectively mitigating the underestimation of

739 *LE* in its original estimates.

740 **5.3 Contributions and implications of this study**

741 The main contributions of this study include: (1) The MEP model's energy balance equation over water

742 surfaces was revised to explicitly consider heat storage effect. This correction highlights the importance of

743 heat storage in estimating *LE*. (2) The energy partitioning of the MEP model was revised to incorporate

744 empirical Bowen ratio formulas, significantly improving the heat flux estimations. (3) This study conducted

745 the first thorough global assessment of heat storage using extensive buoy observations and remote sensed

746 data, enabling the MEP model to produce the most accurate global *LE* estimates. This study addresses the

747 issue of underestimating *LE* by the original MEP model, increasing the global average *LE* from 53 $W \cdot m^{-2}$ to

748 93 $W \cdot m^{-2}$, while reducing sensible heat flux from 25 $W \cdot m^{-2}$ to 12 $W \cdot m^{-2}$, improving the partitioning of energy

749 budget. The improved MEP model provided precise *LE* estimates compared to existing datasets like J-

750 OFURO3, ERA5, MERRA2, and OAFlux, enabling it to become a valuable benchmark dataset for global

751 evaporation studies.

752   From a methodological perspective, the improved MEP method emerged as a novel approach for

753 estimating energy fluxes that diverges from traditional bulk methods. The conventional bulk method requires

754 multiple input parameters, including air temperature, specific humidity, wind speed, sea surface temperature,

755 atmospheric pressure, and the observational height of all parameters (Fairall et al., 2003; Tomita et al., 2021).

756 This method demands numerous input variables, and the estimated fluxes are highly sensitive to changes in

757 temperature and humidity gradients. In contrast, the improved MEP model requires only net radiation, heat

758 storage, surface temperature, and atmospheric pressure to simultaneously obtain latent and sensible heat

759 fluxes, making it more flexible to operate and robust against variations in input variables. Furthermore, the

760 improved MEP model is not constrained by the magnitude of heat storage and theoretically can be applied

761 across various temporal scales (including sub-daily and daily), beyond the monthly scale used in this study.

762 This underscores the applicability of the MEP method in addressing the constraints of traditional bulk

763 methods, providing another independent approach to estimating heat fluxes across diverse environmental

764 conditions.

765   This study applied the improved MEP model to ocean surface, with potential for future extension to lake

766   and reservoir surfaces. Compared to the Penman model for water body evaporation (Tian et al., 2022; Zhao

767   et al., 2022; Bai et al., 2023), the major advantage of MEP method lies in its independence from wind speed,

768   provided that heat storage can be determined using an equilibrium temperature-based approach (McMahon

769   et al., 2013; Zhao & Gao, 2019). The global *LE* dataset generated in this study, due to MEP's insensitivity to

770   variations in air temperature and humidity, can be applied in research related to ocean salinity (Liu et al.,

771   2019), ocean warming (Cheng et al., 2022), and global climate change and water cycle studies (Konapala et

772   al., 2020).

773   ## 5.4 Limitations

774   The improved MEP method proposed in this study offers a novel approach for estimating ocean heat fluxes,

775   producing a validated long-term global dataset with high accuracy and spatiotemporal continuity. Despite its

776   advancements, the proposed MEP method has several limitations that require further refinement: (1)

777   Uncertainty of Driving data: The input variables of net radiation, heat storage, and sea surface temperature

778   for the MEP model were sourced from the state-of-the-art satellite-based J-OFURO3 dataset. This dataset

779   was constructed using observations from multiple satellite sensors. The net radiation in J-OFURO3 was

780   derived by combining data from the CERES and the International Satellite Cloud Climatology Project

781   (ISCCP) via the creeping sea fill method, along with twelve global sea surface temperature products (Tomitta,

782   2019). Consequently, the uncertainty of the MEP-estimated fluxes may arise from biases in input data derived

783   from various satellite sensors and their associated analysis methods. Therefore, it is essential to integrate

784   multiple approaches to assess the uncertainty associated with the input datasets. Moreover, due to the limited

785   temporal duration of the J-OFURO3 dataset, future work should utilize input datasets with longer time series,

786   finer spatio-temporal resolution (Liang et al., 2022), and higher accuracy to advance ocean heat flux

787   estimations using the MEP method. (2) Heat Storage Determination: This study did not employ a direct

788   calculation method to obtain heat storage. Given the unclear relationship between heat storage and changes

789   in ocean heat content at varying depths (as shown in Table 4), we utilized an energy balance residual-based

790   approach to indirectly estimate heat storage. Consequently, this may render the MEP method susceptible to

791   uncertainties in heat storage data derived from auxiliary flux datasets. Future research should focus on

792   understanding the relationship between ocean heat content changes in the upper 100m and heat storage, with

793   the goal of establishing a functional relationship between water column temperature at different depths and

794   heat storage. (3) Bowen Ratio Improvement: Accurate determination of the Bowen ratio in high-latitude

795   regions remains challenging. The Bowen ratio derived from the MEP method showed significant

796   discrepancies with other datasets in these areas (Fig. 10), particularly in sea-ice-covered Arctic regions, where

797   other datasets exhibited notable overestimations and irregular fluctuations. Therefore, incorporating more

798   observational data from high-latitude regions is essential for a better understanding of energy partitioning

799   patterns.

800   ## 6. Data availability

801   The GOHF-MEP dataset produced by the MEP method, which includes global latent heat flux and sensible

802   heat flux at a monthly scale from 1988 to 2017, can be freely downloaded from the Figshare platform

803   (https://doi.org/10.6084/m9.figshare.26861767.v2, Yang et al., 2024). All the datasets used in this study are

804   publicly available online and are described in the "Data Materials" section.

805   ## 7. Conclusions

806   In this study, we developed a new global ocean heat flux product (GOHF-MEP) covering the period from

807   1988 to 2017. This product is grounded in a maximum entropy production theory framework, incorporating

808   heat storage impacts and Bowen ratio adjustments. GOHF-MEP represents the first energy-balance-based

809   dataset that diverges from existing global ocean heat flux datasets derived from bulk methods. To assess the

810   accuracy of the input variables for the maximum entropy production framework, we utilized five global

811   datasets, including two remote sensing-based and three from reanalysis-based, along with four global datasets

812   of heat storage derived from the energy balance equation and ocean heat content changes. We employed data

813   fusion methods, including arithmetic averaging and the Bayesian three-cornered hat method, to identify

814   optimal input datasets through validation against observations. The performance of the newly produced

815   GOHF-MEP dataset was evaluated against extensive observations from 129 globally distributed buoy

816   stations using multiple statistical metrics. It was also compared with four auxiliary products: J-OFURO3,

817   ERA5, MERRA2, and OAFlux. Moreover, we analyzed the long-term spatial-temporal variability of ocean

818   latent heat flux. Ultimately, we investigated the impacts of ocean heat storage, net radiation, and Bowen ratio

819   changes on heat flux estimations and surface energy partitioning.

820   The MEP framework provides new estimates of global heat fluxes. The MEP-estimated long-term

821   annual mean latent heat flux is 93 W·m^{-2} (equivalent to 1196 mm/year of evaporation) during the period from

822   1988 to 2017. This estimate is intermediate compared to other global flux products, which range from 90

823   W·m^{-2} (OAFlux) to 101 W·m^{-2} (MERRA2). The MEP-estimated sensible heat flux is 12 W·m^{-2}, falling within

824   the range of 10.17 W·m^{2} (J-OFURO3) to 13 W·m^{2} (MERRA2) reported by other current products. Compared

825   with previous heat flux products, the MEP-estimated latent heat demonstrated higher accuracy when

826   validated against observations, with a ME of 1.26 W·m^{-2}, a RMSE of 16 W·m^{-2}, and a KGE value of 0.89,

827   outperforming all other contemporary global products. Approximately 74% of oceanic regions experienced

828   an increasing trend in evaporation from 1988 to 2017. In terms of long-term temporal variability, the global

829   annual mean evaporation exhibited an increase rate of 3.58 mm/year from 1988 to 2010 but subsequently

830   declined at a rate of 2.18 mm/year from 2010 to 2017, which was consistent with changes in surface available

831   energy.

832   This study demonstrates that the improved MEP framework has significantly improved the accuracy of

833   the original MEP theory, addressing both the underestimation of latent heat and the overestimation of sensible

834   heat flux. This improvement was achieved by incorporating the impact of heat storage and modifying the

835   Bowen ratio formula within the MEP theory. The consideration of heat storage resolved the issue of seasonal

836   phase mismatches (approximately 6-month lags) between MEP estimates and buoy observations. Building

837   upon this improvement, this study further optimized the energy partitioning process by correcting the Bowen

838   ratio, linearly adjusting the equilibrium Bowen ratio to align with actual conditions. Four empirical Bowen

839   ratio formulas for modifying the MEP method were assessed globally, identifying $B_{oa}=0.24B_o^*$ as the most

840   accurate formula for estimating latent heat flux within MEP method. The impact of heat storage on estimating

841   heat fluxes was quantified through sensitivity analysis. Net radiation and heat storage were identified as the

842   primary drivers of evaporation estimates. A 10% decrease in positive heat storage led to a 7.4% increase in

843   evaporation, whereas a 10% increase in negative heat storage resulted in a 2.9% increase.

844   Compared to existing bulk methods, the MEP model offers several advantages, including the

845   requirement for fewer input variables, independence from wind speed, and insensitivity to variations in

temperature and humidity. The MEP-derived ocean heat flux dataset has been validated and provides accurate estimates of latent heat flux. Additionally, this MEP method can be applied to estimate evaporation from other deep-water surfaces, such as lakes and reservoirs where heat storage is significant. Overall, the MEP-derived ocean heat flux dataset provides high global accuracy, fine spatial resolution (0.25°), and extensive long-term temporal records. This dataset is expected to be valuable for applications related to global ocean warming, hydrological cycles, and their interactions with other Earth system components in the context of climate change.

Supplement. The Supplementary material related to this article is submitted during submission.

Author contributions. YY and HS developed the methodology and designed the experiments, WZ contributed the conceptual design, YY and WZ collected and processed the data, YY wrote the first draft of the paper under the supervision of other authors. All authors participated in the revising and editing of the manuscript.

Competing interests. The contact author has declared that none of the authors has any competing interests.

Acknowledgments. We acknowledge the GTMBA Project Office of NOAA/PMEL for providing the Global Tropical Moored Buoy Array observations. This study was primarily funded by the Third Xinjiang Scientific Expedition Program (Grant No.2022xjkk0105) (H.S.). The authors acknowledge funding from the NSFC project (52079055, 52011530128). H.S. and W.Z. acknowledges funding from the NSFC-STINT projects (No. 202100-3211 and CH2019-8281). W.Z. was supported by the grants from Swedish Research Council VR (2020-05338), and Swedish National space Agency (209/19).

870 **References**

871 Andreas, E. L., & Cash, B. A.: A new formulation for the Bowen ratio over saturated surfaces. Journal of
872   Applied Meteorology and Climatology, 35(8), 1279-1289, https://doi.org/10.1175/1520-
873   0450(1996)035%3C1279:ANFFTB%3E2.0.CO;2, 1996.

874 Andreas, E. L., Jordan, R. E., Mahrt, L., & Vickers, D.: Estimating the Bowen ratio over the open and ice-
875   covered ocean. Journal of Geophysical Research: Oceans, 118(9), 4334-4345,
876   https://doi.org/10.1002/jgrc.20295, 2013.

877 Andreas, E. L., Persson, P. O. G., & Hare, J. E.: A bulk turbulent air–sea flux algorithm for high-wind, spray
878   conditions. Journal of Physical Oceanography, 38(7), 1581-1596,
879   https://doi.org/10.1175/2007JPO3813.1, 2008.

880 Bai, P., & Guo, X.: Development of a 60-year high-resolution water body evaporation dataset in China.
881   Agricultural and Forest Meteorology, 334, 109428, https://doi.org/10.1016/j.agrformet.2023.109428,
882   2023.

883 Bai, P., & Wang, Y.: The importance of heat storage for estimating lake evaporation on different time scales:
884   Insights from a large shallow subtropical lake. Water Resources Research, 59, e2023WR035123.
885   https://doi.org/10.1029/2023WR035123, 2023.

886 Bentamy, A., Piolle, J. F., Grouazel, A., Danielson, R., Gulev, S., Paul, F., ... & Josey, S. A.: Review and
887   assessment of latent and sensible heat flux accuracy over the global oceans. Remote Sensing of
888   Environment, 201, 196-218, https://doi.org/10.1016/j.rse.2017.08.016, 2017.

889 Beven, K.: A sensitivity analysis of the Penman-Monteith actual evapotranspiration estimates. Journal of
890   Hydrology, 44(3–4), 169-190, https://doi.org/10.1016/0022-1694(79)90130-6, 1979.

891 Bosilovich, M. G., Robertson, F. R., & Chen, J.: Global energy and water budgets in MERRA. Journal of
892   Climate, 24(22), 5721-5739, https://doi.org/10.1175/2011JCLI4175.1, 2011.

893 Bourras, D.: Comparison of five satellite-derived latent heat flux products to moored buoy data. Journal of
894   Climate, 19(24), 6291-6313, https://doi.org/10.1175/JCLI3977.1, 2006.

895 Chen, X., Yao, Y., Li, Y., Zhang, Y., Jia, K., Zhang, X., ... & Guo, X.: ANN-based estimation of low-latitude
896   monthly ocean latent heat flux by ensemble satellite and reanalysis products. Sensors, 20(17), 4773,
897   https://doi.org/10.3390/s20174773, 2020.

898 Cheng, L., Pan, Y., Tan, Z., Zheng, H., Zhu, Y., Wei, W., ... & Zhu, J.: IAPv4 ocean temperature and ocean
899   heat content gridded dataset. Earth System Science Data Discussions, 1-56,
900   https://doi.org/10.5194/essd-16-3517-2024, 2024.

901 Cheng, L., Trenberth, K. E., Fasullo, J., Boyer, T., Abraham, J., & Zhu, J.: Improved estimates of ocean heat
902   content from 1960 to 2015. Science Advances, 3(3), e1601545, https://doi.org/10.1126/sciadv.1601545,
903   2017.

904 Cheng, L., von Schuckmann, K., Abraham, J. P., Trenberth, K. E., Mann, M. E., Zanna, L., ... & Lin, X.: Past
905   and future ocean warming. Nature Reviews Earth & Environment, 3(11), 776-794,
906   https://doi.org/10.1038/s43017-022-00345-1, 2022.

907   Duan, S. B., Zhou, S., Li, Z. L., Liu, X., Chang, S., Liu, M., ... & Shang, G.: Improving monthly mean land
908   surface temperature estimation by merging four products using the generalized three-cornered hat
909   method and maximum likelihood estimation. Remote Sensing of Environment, 302, 113989,
910   https://doi.org/10.1016/j.rse.2023.113989, 2024.

911   Fairall, C. W., Bradley, E. F., Hare, J. E., Grachev, A. A., & Edson, J. B.: Bulk parameterization of air–sea
912   fluxes: Updates and verification for the COARE algorithm. Journal of climate, 16(4), 571-591,
913   https://doi.org/10.1175/1520-0442(2003)016%3C0571:BPOASF%3E2.0.CO;2, 2003.

914   Fairall, C. W., Bradley, E. F., Rogers, D. P., Edson, J. B., & Young, G. S.: Bulk parameterization of air-sea
915   fluxes for tropical ocean-global atmosphere coupled-ocean atmosphere response experiment. Journal of
916   Geophysical Research: Oceans, 101(C2), 3747-3764, https://doi.org/10.1029/95JC03205, 1996.

917   Gelaro, R., McCarty, W., Suárez, M. J., Todling, R., Molod, A., Takacs, L., ... & Zhao, B.: The modern-era
918   retrospective analysis for research and applications, version 2 (MERRA-2). Journal of climate, 30(14),
919   5419-5454, https://doi.org/10.1175/JCLI-D-16-0758.1, 2017.

920   Guo, J., Li, W., Chang, X., Zhu, G., Liu, X., & Guo, B.: Terrestrial water storage changes over Xinjiang
921   extracted by combining Gaussian filter and multichannel singular spectrum analysis from GRACE.
922   Geophysical Journal International, 213(1), 397-407, https://doi.org/10.1093/gji/ggy006, 2018.

923   He, X., Xu, T., Xia, Y., Bateni, S. M., Guo, Z., Liu, S., ... & Zhao, J.: A Bayesian three-cornered hat (BTCH)
924   method: improving the terrestrial evapotranspiration estimation. Remote Sensing, 12(5), 878,
925   https://doi.org/10.3390/rs12050878, 2020.

926   Hersbach, H., Bell, B., Berrisford, P., Hirahara, S., Horányi, A., Muñoz-Sabater, J., ... & Thépaut, J. N.: The
927   ERA5 global reanalysis. Quarterly Journal of the Royal Meteorological Society, 146(730), 1999-2049,
928   https://doi.org/10.1002/qj.3803, 2020.

929   Hicks, B. B., & Hess, G. D.: On the Bowen ratio and surface temperature at sea. Journal of physical
930   oceanography,   7(1),   141-145,   https://doi.org/10.1175/1520-
931   0485(1977)007%3C0141:OTBRAS%3E2.0.CO;2, 1977.

932   Huang, S. Y., Deng, Y., & Wang, J.: Revisiting the global surface energy budgets with maximum-entropy-
933   production   model   of   surface   heat   fluxes.   Climate   Dynamics,   49,   1531-1545,
934   https://link.springer.com/article/10.1007/s00382-016-3395-x, 2017.

935   Isabelle, P. E., Viens, L., Nadeau, D. F., Anctil, F., Wang, J., & Maheu, A.: Sensitivity analysis of the
936   maximum entropy production method to model evaporation in boreal and temperate forests.
937   Geophysical Research Letters, 48(13), e2020GL091919, https://doi.org/10.1029/2020GL091919, 2021.

938   Iwasaki, S., Kubota, M., & Watabe, T.: Assessment of various global freshwater flux products for the global
939   ice-free   oceans.   Remote   sensing   of   environment,   140,   549-561,
940   https://doi.org/10.1016/j.rse.2013.09.026, 2014.

941   Jo, Y. H., Yan, X. H., Pan, J., He, M. X., & Liu, W. T.: Calculation of the Bowen ratio in the tropical Pacific
942   using sea surface temperature data. Journal of Geophysical Research: Oceans, 107(C9), 17-1,
943   https://doi.org/10.1029/2001JC001150, 2002.

944 Johnson, G. C., & Lyman, J. M.: Warming trends increasingly dominate global ocean. Nature Climate
945   Change, 10(8), 757-761, https://doi.org/10.1038/s41558-020-0822-0, 2020.

946 Konapala, G., Mishra, A. K., Wada, Y., & Mann, M. E.: Climate change will affect global water availability
947   through compounding changes in seasonal precipitation and evaporation. Nature communications, 11(1),
948   3044, https://doi.org/10.1038/s41467-020-16757-w, 2020.

949 Lenhart, T., Eckhardt, K., Fohrer, N., & Frede, H. G.: Comparison of two different approaches of sensitivity
950   analysis. Physics and Chemistry of the Earth, Parts A/B/C, 27(9-10), 645-654,
951   https://doi.org/10.1016/S1474-7065(02)00049-9, 2002.

952 Li, Z., England, M. H., & Groeskamp, S.: Recent acceleration in global ocean heat accumulation by mode
953   and intermediate waters. Nature Communications, 14(1), 6888, https://doi.org/10.1038/s41467-023-
954   42468-z, 2023.

955 Liang, H., Jiang, B., Liang, S., Peng, J., Li, S., Han, J., ... & Zhang, X.: a global long-term ocean surface
956   daily/0.05 net radiation product from 1983–2020. Scientific Data, 9(1), 337,
957   https://doi.org/10.1038/s41597-022-01419-x, 2022.

958 Liu, C., Liang, X., Ponte, R. M., Vinogradova, N., & Wang, O.: Vertical redistribution of salt and layered
959   changes in global ocean salinity. Nature communications, 10(1), 3445, https://doi.org/10.1038/s41467-
960   019-11436-x, 2019.

961 Liu, J., Chai, L., Dong, J., Zheng, D., Wigneron, J. P., Liu, S., ... & Lu, Z.: Uncertainty analysis of eleven
962   multisource soil moisture products in the third pole environment based on the three-corned hat method.
963   Remote sensing of environment, 255, 112225, https://doi.org/10.1016/j.rse.2020.112225, 2021.

964 Liu, Z., & Yang, H.: Estimation of water surface energy partitioning with a conceptual atmospheric boundary
965   layer model. Geophysical Research Letters, 48(9), e2021GL092643,
966   https://doi.org/10.1029/2021GL092643, 2021.

967 Long, D., Pan, Y., Zhou, J., Chen, Y., Hou, X., Hong, Y., ... & Longuevergne, L.: Global analysis of
968   spatiotemporal variability in merged total water storage changes using multiple GRACE products and
969   global hydrological models. Remote sensing of environment, 192, 198-216,
970   https://doi.org/10.1016/j.rse.2017.02.011, 2017.

971 Marti, F., Blazquez, A., Meyssignac, B., Ablain, M., Barnoud, A., Fraudeau, R., ... & Benveniste, J.:
972   Monitoring the ocean heat content change and the Earth energy imbalance from space altimetry and
973   space gravimetry. Earth System Science Data, 14(1), 229-249, https://doi.org/10.5194/essd-14-229-
974   2022, 2022.

975 Masson-Delmotte V, Zhai P, Pirani S, Connors C, Péan S, Berger N, et al.: IPCC, 2021: Summary for
976   policymakers. in: Climate change 2021: The physical science basis. contribution of working group I to
977   the sixth assessment report of the intergovernmental panel on climate change, pp.3−32,
978   doi:10.1017/9781009157896.001, 2021.

979 McMahon, T. A., Peel, M. C., Lowe, L., Srikanthan, R., & McVicar, T. R.: Estimating actual, potential,
980   reference crop and pan evaporation using standard meteorological data: a pragmatic synthesis.

981 Hydrology and Earth System Sciences, 17(4), 1331-1363, https://doi.org/10.5194/hess-17-1331-2013,
982 2013.

983 Medhaug, I., Stolpe, M. B., Fischer, E. M., & Knutti, R.: Reconciling controversies about the 'global warming
984 hiatus'. Nature, 545 (7652), 41-47, https://doi.org/10.1038/nature22315, 2017.

985 Meehl, G. A.: A calculation of ocean heat storage and effective ocean surface layer depths for the Northern
986 Hemisphere. Journal of physical oceanography, 14(11), 1747-1761, https://doi.org/10.1175/1520-
987 0485(1984)014<1747:ACOOHS>2.0.CO;2, 1984.

988 Morton, F. I.: Evaporation research—a critical review and its lessons for the environmental sciences. Critical
989 Reviews in Environmental Science and Technology, 24(3), 237–280.
990 https://doi.org/10.1080/10643389409388467, 1994.

991 Pelletier, C., Lemarié, F., & Blayo, E.: Sensitivity analysis and metamodels for the bulk parametrization of
992 turbulent air–sea fluxes. Quarterly Journal of the Royal Meteorological Society, 144(712), 658-669,
993 https://doi.org/10.1002/qj.3233, 2018.

994 Philip, J.R.: A physical bound on the Bowen ratio. Journal of Climate and Applied Meteorology, 26, 1043–
995 1045, https://doi.org/10.1175/1520-0450(1987)026%3C1043:APBOTB%3E2.0.CO;2, 1987.

996 Pinker, R. T., & Laszlo, I.: Modeling surface solar irradiance for satellite applications on a global scale.
997 Journal of Applied Meteorology and Climatology, 31(2), 194-211, https://doi.org/10.1175/1520-
998 0450(1992)031%3C0194:MSSIFS%3E2.0.CO;2, 1992.

999 Pokhrel, S., Dutta, U., Rahaman, H., Chaudhari, H., Hazra, A., Saha, S. K., & Veeranjaneyulu, C.: Evaluation
1000 of different heat flux products over the tropical Indian Ocean. Earth and Space Science, 7(6),
1001 e2019EA000988, https://doi.org/10.1029/2019EA000988, 2020.

1002 Priestley, C. H. B., & Taylor, R. J.: On the assessment of surface heat flux and evaporation using large-scale
1003 parameters. Monthly weather review, 100(2), 81-92, https://doi.org/10.1175/1520-
1004 0493(1972)100%3C0081:OTAOSH%3E2.3.CO;2, 1972.

1005 Robertson, F. R., Roberts, J. B., Bosilovich, M. G., Bentamy, A., Clayson, C. A., Fennig, K., ... & Slivinski,
1006 L. C.: Uncertainties in ocean latent heat flux variations over recent decades in satellite-based estimates
1007 and reduced observation reanalyses. Journal of Climate, 33(19), 8415-8437,
1008 https://doi.org/10.1175/JCLI-D-19-0954.1, 2020.

1009 Roderick, M. L., Sun, F., Lim, W. H., & Farquhar, G. D.: A general framework for understanding the response
1010 of the water cycle to global warming over land and ocean. Hydrology and Earth System Sciences, 18(5),
1011 1575-1589, https://doi.org/10.5194/hess-18-1575-2014, 2014.

1012 Rutan, D. A., Kato, S., Doelling, D. R., Rose, F. G., Nguyen, L. T., Caldwell, T. E., & Loeb, N. G.: CERES
1013 synoptic product: Methodology and validation of surface radiant flux. Journal of Atmospheric and
1014 Oceanic Technology, 32(6), 1121-1143, https://doi.org/10.1175/JTECH-D-14-00165.1, 2015.

1015 Shaman, J., & Kohn, M.: Absolute humidity modulates influenza survival, transmission, and seasonality.
1016 Proceedings of the National Academy of Sciences, 106(9), 3243-3248, DOI: 10.1073/pnas.0806852106,
1017 2009.

Shao, X., Zhang, Y., Liu, C., Chiew, F. H., Tian, J., Ma, N., & Zhang, X.: Can indirect evaluation methods and their fusion products reduce uncertainty in actual evapotranspiration estimates?. Water Resources Research, 58(6), e2021WR031069, https://doi.org/10.1029/2021WR031069, 2022.

Smith, S. R., Hughes, P. J., & Bourassa, M. A.: A comparison of nine monthly air–sea flux products. International Journal of Climatology, 31(7), 1002-1027, https://doi.org/10.1002/joc.2225, 2011.

Sun, H., Chen, J., Yang, Y., Yan, D., Xue, J., Wang, J., & Zhang, W.: Assessment of long-term water stress for ecosystems across China using the maximum entropy production theory-based evapotranspiration product. Journal of Cleaner Production, 349, 131414, https://doi.org/10.1016/j.jclepro.2022.131414, 2022.

Sun, H., Sun, X., Chen, J., Deng, X., Yang, Y., Qin, H., ... & Zhang, W.: Different types of meteorological drought and their impact on agriculture in Central China. Journal of Hydrology, 627, 130423, https://doi.org/10.1016/j.jhydrol.2023.130423, 2023.

Sung, M. K., An, S. I., Shin, J., Park, J. H., Yang, Y. M., Kim, H. J., & Chang, M: Ocean fronts as decadal thermostats modulating continental warming hiatus. Nature communications, 14(1), 7777, https://doi.org/10.1038/s41467-023-43686-1, 2023.

Tang, R., Wang, Y., Jiang, Y., Liu, M., Peng, Z., Hu, Y., ... & Li, Z. L.: A review of global products of air-sea turbulent heat flux: accuracy, mean, variability, and trend. Earth-Science Reviews, 104662, https://doi.org/10.1016/j.earscirev.2023.104662, 2023.

Tian, W., Liu, X., Wang, K., Bai, P., Liu, C., & Liang, X.: Estimation of global reservoir evaporation losses. Journal of Hydrology, 607, 127524, https://doi.org/10.1016/j.jhydrol.2022.127524, 2022.

Tomita, H., Hihara, T., & Kubota, M.: Improved satellite estimation of near-surface humidity using vertical water vapor profile information. Geophysical Research Letters, 45(2), 899-906, https://doi.org/10.1002/2017GL076384, 2018.

Tomita, H., Hihara, T., Kako, S. I., Kubota, M., & Kutsuwada, K.: An introduction to J-OFURO3, a third-generation Japanese ocean flux data set using remote-sensing observations. Journal of Oceanography, 75(2), 171-194, https://doi.org/10.1007/s10872-018-0493-x, 2019.

Tomita, H., Kutsuwada, K., Kubota, M., & Hihara, T.: Advances in the estimation of global surface net heat flux based on satellite observation: J-OFURO3 V1. 1. Frontiers in Marine Science, 8, 612361, https://doi.org/10.3389/fmars.2021.612361, 2021.

Von Schuckmann, K., Minière, A., Gues, F., Cuesta-Valero, F. J., Kirchengast, G., Adusumilli, S., ... & Zemp, M.: Heat stored in the Earth system 1960–2020: where does the energy go?. Earth System Science Data, 15(4), 1675-1709, https://doi.org/10.5194/essd-15-1675-2023, 2023.

Wang, J., & Bras, R. L.: A model of evapotranspiration based on the theory of maximum entropy production. Water Resources Research, 47(3), https://doi.org/10.1029/2010WR009392, 2011.

Wang, J., & Bras, R. L.: An extremum solution of the Monin–Obukhov similarity equations. Journal of the atmospheric sciences, 67(2), 485-499, https://doi.org/10.1175/2009JAS3117.1, 2010.

1054   Wang, J., Bras, R. L., Nieves, V., & Deng, Y.: A model of energy budgets over water, snow, and ice surfaces.
1055   Journal of Geophysical Research: Atmospheres, 119(10), 6034-6051, https://doi.org/10.1002/2013JD021150, 2014.

1057   Wang, K., & Dickinson, R. E.: A review of global terrestrial evapotranspiration: Observation, modeling,
1058   climatology, and climatic variability. Reviews of Geophysics, 50(2), https://doi.org/10.1029/2011RG000373, 2012.

1060   Wang, W., Chakraborty, T. C., Xiao, W., & Lee, X.: Ocean surface energy balance allows a constraint on the
1061   sensitivity of precipitation to global warming. Nature Communications, 12(1), 2115, https://doi.org/10.1038/s41467-021-22406-7, 2021.

1063   Wentz, F. J., Ricciardulli, L., Hilburn, K., & Mears, C.: How much more rain will global warming bring?.
1064   Science, 317(5835), 233-235, DOI:10.1126/science.1140746, 2007.

1065   Wielicki, B. A., Barkstrom, B. R., Harrison, E. F., Lee III, R. B., Smith, G. L., & Cooper, J. E.: Clouds and
1066   the Earth's Radiant Energy System (CERES): An earth observing system experiment. Bulletin of the
1067   American Meteorological Society, 77(5), 853-868, https://doi.org/10.1175/1520-0477(1996)077%3C0853:CATERE%3E2.0.CO;2, 1996.

1069   Xu, T., Guo, Z., Xia, Y., Ferreira, V. G., Liu, S., Wang, K., ... & Zhao, C.: Evaluation of twelve
1070   evapotranspiration products from machine learning, remote sensing and land surface models over
1071   conterminous United States. Journal of Hydrology, 578, 124105, https://doi.org/10.1016/j.jhydrol.2019.124105, 2019.

1073   Yang, Y., & Roderick, M. L.: Radiation, surface temperature and evaporation over wet surfaces. Quarterly
1074   Journal of the Royal Meteorological Society, 145(720), 1118–1129, https://doi.org/10.1002/qj.3481, 2019.

1076   Yang, Y., Roderick, M. L., Guo, H., Miralles, D. G., Zhang, L., Fatichi, S., ... & Yang, D.: Evapotranspiration
1077   on a greening Earth. Nature Reviews Earth & Environment, 4(9), 626-641, https://doi.org/10.1038/s43017-023-00464-3, 2023.

1079   Yang, Y., Sun, H., Zhu, M., Wang, J., & Zhang, W.: An R package of maximum entropy production model
1080   to estimate 41 years of global evapotranspiration. Journal of Hydrology, 614, 128639, https://doi.org/10.1016/j.jhydrol.2022.128639, 2022.

1082   Yin, Y., Wu, S., Chen, G., & Dai, E.: Attribution analyses of potential evapotranspiration changes in China
1083   since the 1960s. Theoretical and applied climatology, 101, 19-28, https://doi.org/10.1007/s00704-009-0197-7, 2010.

1085   Yu, L., X. Jin, and R. A. Weller.: Multidecade Global Flux Datasets from the Objectively Analyzed Air-sea
1086   Fluxes (OAFlux) Project: Latent and sensible heat fluxes, ocean evaporation, and related surface
1087   meteorological variables. Woods Hole Oceanograp, 2008.

1088   Yu, L.: A global relationship between the ocean water cycle and near-surface salinity. Journal of Geophysical
1089   Research: Oceans, 116(C10), https://doi.org/10.1029/2010JC006937, 2011.

1090   Zeng, X., Zhao, M., & Dickinson, R. E.: Intercomparison of bulk aerodynamic algorithms for the
1091   computation of sea surface fluxes using TOGA COARE and TAO data. Journal of Climate, 11(10),
1092   2628-2644, https://doi.org/10.1175/1520-0442(1998)011%3C2628:IOBAAF%3E2.0.CO;2, 1998.

1093   Zhao, G., & Gao, H.: Estimating reservoir evaporation losses for the United States: Fusing remote sensing
1094   and modeling approaches. Remote Sensing of Environment, 226, 109-124,
1095   https://doi.org/10.1016/j.rse.2019.03.015, 2019.

1096   Zhao, G., Gao, H., Naz, B. S., Kao, S. C., & Voisin, N.: Integrating a reservoir regulation scheme into a
1097   spatially distributed hydrological model. Advances in Water Resources, 98, 16-31,
1098   https://doi.org/10.1016/j.advwatres.2016.10.014, 2016.

1099   Zhao, G., Li, Y., Zhou, L., & Gao, H.: Evaporative water loss of 1.42 million global lakes. Nature
1100   Communications, 13(1), 3686, https://doi.org/10.1038/s41467-022-31125-6, 2022.